Transformation Optics for Plasmonics

Alexandre Aubry, John B Pendry

Transformation Optics for Plasmonics

Alexandre Aubry
ESPCI ParisTech, PSL Research University, CNRS, Univ Paris Diderot, Sorbonne Paris Cité, Institut Langevin, UMR 7587, 1 rue Jussieu, F-75005 Paris, France

John B. Pendry
Blackett Laboratory, Department of Physics, Imperial College London, London SW7 2AZ, UK

I. INTRODUCTION

Since the pioneering work of Mie [1] and Ritchie [2], there has been a vast amount of research effort to investigate the electromagnetic (EM) properties of metal/dielectric interfaces (see *e.g* [3–6] and references therein). Surface plasmon polaritons (SPPs) can show strong coupling to light and have wavelength of only a few tens of nanometers, hence beating the classical diffraction limit [7, 8]. In particular, localized surface plasmons (LSPs) can be excited in a metal particle and give rise to a local enhancement of the EM field. In the literature, the maximization of the field enhancement is generally obtained by combining the strong overall resonance of the plasmonic structure with very small and sharp geometric features where hot spots arise. Following this principle, several plasmonic structures have been investigated, such that triangles/squares with sharp corners [9, 10], nanoparticle dimers [10–24], crescent-shaped nanoparticles [25–32] or nanoshells [33–38]. The significant field enhancement, that such structures may provide, has drawn a considerable attention in surface enhanced Raman spectroscopy [16, 25, 39–42] or enhanced fluorescent emission [43, 44]. Until now, the theoretical description of the optical response of such structures has remained a challenge: numerical simulations are generally performed and few qualitative arguments are proposed to explain these numerical results. An elegant physical picture to describe the interaction of LSPs in dimers or nanoshells is the plasmon hybridization model [15, 36]. In analogy with molecular orbital theory, the dimer plasmons can be viewed as bonding and antibonding combinations of the individual nanoparticle plasmons. However, albeit elegant, the plasmon hybridization picture is a limited tool: numerical simulations are still needed to calculate the optical response of a dimer. Another severe challenge for potential applications lies in the spectrum bandwidth over which plasmonic particles can efficiently operate. Indeed, small devices tend to be efficient collectors at just a few resonant frequencies, contrary to an infinite structure that naturally shows a broadband spectrum [6]. Nevertheless, transformation optics (TO) can take up this challenge by leading to the design of broadband plasmonic nanostructures acting as strong field concentrators [45].

TO has been used as a tool in electromagnetic design for some time [46–48] and has drawn considerable attention in the last six years sparked by the seminal works of Leonhardt [49] and Pendry [50]. Whereas the Leonhardt approach approximates Maxwell's equations by the Helmhotz equation which is restricted to the far field, the latter approach is exact at the level of Maxwell's equations and can be deployed to treat both near and far fields, and has even been applied to static fields. In this review we are concerned with near field applications.

The paths of EM waves can be controlled by devising a material whose constitutive parameters should vary spatially in a way prescribed by coordinate transformations. Various applications have been proposed and implemented experimentally, among which the famous EM cloak [51–56]. This strategy has been recently extended to plasmonics [57–64]. At visible and infrared frequencies, most of the energy of SPPs is contained in the dielectric layer adjacent to the metal slab. Hence, by devising the optical parameters of the dielectric placed on top of a metal surface, one can design plasmonic devices capable of different functionalities such as beam shifting, waveguide bending, cloaking or focusing. Following this strategy, plasmonic Luneburg and Eaton lenses have been implemented experimentally at optical frequencies [60]. The carpet-cloak concept [52] has also been extended to plasmonics and tested experimentally in the visible regime [59, 64].

In a series of papers [45, 65–76], an alternative strategy based on TO has been proposed for plasmonics. It consists in designing and studying analytically plasmonic devices capable of

- an efficient harvesting of light over a broadband spectrum both in the visible and the near infrared regimes
- a strong far-field to near-field conversion of energy, leading to a considerable field confinement and enhancement.

The strategy is as follows: start with an infinite plasmonic system that naturally shows a broadband spectrum and then apply a mathematical transformation that converts the infinite structure into a finite one while preserving the spectrum [45]. TO provides us with a very general set of transformations but here we shall concentrate on a specific subset: the conformal transformations (CT) [77]. Both the electrostatic potentials and the material permittivity are preserved under 2D conformal mapping. Hence, it does not require the delicate design of a metamaterial with a spatial variation in its constitutive parameters. Note that conformal mapping has also been used in the past to study the electrostatic interaction between dielectric or metallic particles in the context of effective medium theory [78–82]. Following the CT strategy, various broadband plasmonic structures have been designed and studied analytically, such as 2D crescents [65, 71], kissing nanowires [70], touching spheres [67], groove/wedge-like plasmonic

structures [65], nanoparticle dimers [66, 73] or rough surfaces[75]. All these structures have in common to display geometrical singularities that allow simultaneously a broadband interaction with the incoming light as well as a spectacular nanofocusing of its energy.

Despite the power and elegance of the CT approach, one could claim that these theoretical predictions will be difficult to retrieve experimentally. First, the singular structures derived from the CT approach will suffer from inevitable imperfections due to the nanofabrication process. This issue has been solved in a recent paper [68]. Blunt-ended nanostructures can also be derived *via* CT and the possibility of designing devices with an absorption property insensitive to the geometry bluntness has been demonstrated. Second, the CT approach relies on the quasi-static approximation. Its range of application should be restricted to plasmonic devices whose dimension is at least one order of magnitude smaller than the wavelength (typically 40 nm in the optical regime). However, a conformal map of radiative losses allows to go beyond the electrostatic approximation and extend the range of validity of the CT approach until a nanostructure dimension of 200 nm [72]. The third potential limitation of the CT approach is non-locality. The spatial extent of the EM fields in singular structures is comparable to the Coulomb screening length in noble metals, hence non-local effects can be important in the vicinity of the structure singularity. A recent study has shown how non-locality can be taken into account by conformal mapping [69]. A conpromise can be found between radiative losses and non-local effects by adjusting the nanostructure dimension such that the absorption band width and field enhancement capabilities of the nanostructure are maximized.

In this chapter, we review the main designs provided by the CT approach and present the corresponding analytical predictions. The first section presents the general strategy and the three families of nanostructures that one can derive *via* conformal mapping: the perfectly singular plasmonic devices, the singular nanostructures and the resonant ones. In Sec.III and IV, the broadband light harvesting and nanofocusing properties of singular structures are investigated. The vertex angle, which characterizes the strength of the singularity, is shown to be a key parameter. The conformal picture also provides novel physical insights on the formation of hot spots in the vicinity of the structure singularities. The issue of the nanostructure bluntness will also be addressed. The fourth section is dedicated to resonant nanostructures. The plasmonic hybridization model is revisited with TO and a full-analytical solution is provided for 2D nanostructures. In Sec.VI, we show how to take into account radiative losses in the CT approach. Besides being capable to predict analytically the optical properties of nanostrutures until a dimension of 200 nm, the fluorescence enhancement of a molecule as well as its quantum yield can be predicted analytically in the vicinity of complex nanostructures. At last, the CT strategy is refined to investigate the impact that non-locality has on the optical properties of plasmonic nanostructures.

II. THE CONFORMAL TRANSFORMATION APPROACH

A conformal map is an analytic transformation $z' = f(z)$ that preserves local angles [77]. If we consider an analytic function $\phi(z)$ in the complex plane with $z = x + iy$, it will satisfy

$$\frac{\partial^2 \phi}{\partial x^2} + \frac{\partial^2 \phi}{\partial y^2} = 0 \tag{1}$$

If we now make a coordinate transformation $z' = x' + iy' = f(z)$, $\phi(z')$ also satisfies the Laplace equation in the new coordinate system:

$$\frac{\partial^2 \phi}{\partial x'^2} + \frac{\partial^2 \phi}{\partial y'^2} = 0 \tag{2}$$

provided that the transformation is everywhere analytic in the region under consideration. Hence, in 2D electrostatics, a CT preserves the potential in each coordinate system:

$$\phi(x, y) = \phi'(x', y') \tag{3}$$

Moreover, the continuities of the tangential component of the electric field $E_{||}$ and of the normal component of the displacement current $D_\perp = \epsilon E_\perp$ across a boundary are also conserved due to the preservation of local angles. Thus, the permittivity of each material is the same in each geometry:

$$\epsilon(x, y) = \epsilon(x', y') \tag{4}$$

On the one hand, the CT approach allows a tractable analytical study of complex structures, in contrast with full-wave coordinate transformations that generally imply strong spatial variations and anisotropy for the constitutive parameters. On the other hand, the CT approach is only valid in the quasi-static approximation: the plasmonic structures that we will deduce by conformal mapping should be one order of magnitude smaller than the wavelength. However, we will show in Sec.VI how to go beyond the quasi-static limit and take into account radiative losses in the CT picture.

The strategy of our approach is as follows: start with an infinite plasmonic system that generally shows a broadband spectrum and apply a mathematical transformation that converts the infinite structure into a finite one whilst preserving the spectrum. We will start by describing a set of canonic structures easily tractable analytically on which we will then apply an ensemble of transformations.

A. A set of canonic plasmonic structures

The set of infinite plasmonic structures displayed in Fig.1 correspond to the initial geometries used for the CT approach. Fig.1(a) and (b) correspond to the classical insulator-metal-insulator (IMI) and metal-insulator-metal (MIM) structures widely studied in plasmonics [5]. A 2D dipole pumps energy into the SP modes of the metallic slab(s) that transport the energy out to infinity. Although the SP spectrum of a plane surface is degenerate at ω_{sp}, the SP frequency, in a thin slab, hybridization of SPs on opposing surfaces creates a continuous spectrum with a lower bound at zero frequency and an upper bound at the bulk plasma frequency ω_p. Conformal mapping of such structures will give rise to a set of perfectly singular metallic structures (kissing nanowires, 2D crescent with touching tips *etc.*) capable of an efficient harvesting and a strong nanofocusing of light over a broadband spectrum [45] (see Sec.II B).

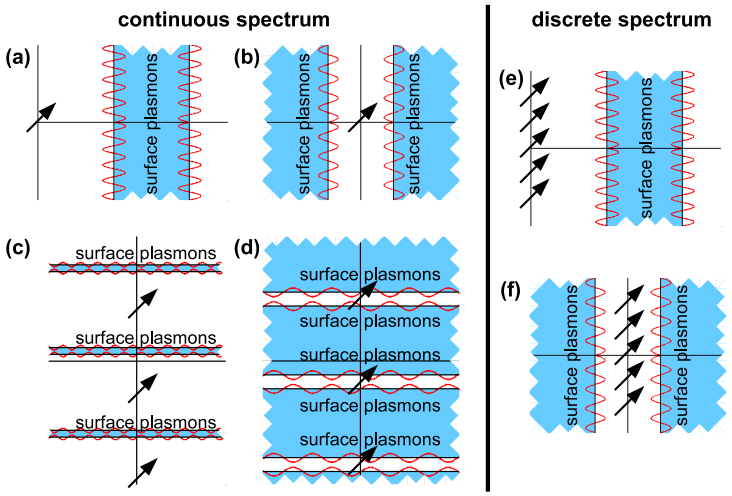

FIG. 1: A set of canonical structures. A thin layer of metal (a) and two semi-infinite metallic slabs separated by a thin dielectric film (b) support SPs that couple to a 2D dipole source, transporting its energy to infinity. (c)-(d) An infinite and periodic stack of metallic slabs separated by dielectric layers can support hybridized SPs excited by an array of line dipoles. (e)-(f) The SP modes of the IMI and MIM structures are now excited by an array of 2D dipoles.

The CT is not only dedicated to the design of broadband plasmonic nanostructures. It can also generate resonant nanostructures. To that aim, an array of 2D dipoles can be used to excite SPs in IMI and MIM geometries (see Fig.1(e)-(f)). In that case, SPs can only be excited at certain resonant frequencies fixed by the pitch of the dipole array. Such a structure will give rise after conformal mapping to resonant nanostructures, such as metallic dimers [10–13, 15, 17, 18, 20–22, 24], 2D nanoshells [33–38] or a nanowire placed on top of metal plate [39, 42, 83–85], that have been widely studied both numerically and experimentally in plasmonics (see Sec.II D).

At last, more exotic structures can be studied like the one shown in Fig.1(c)-(d). A periodic and infinite stack of metallic slabs supports hybridized SPs over a broadband spectrum. The latter ones are excited by an infinite array of dipoles placed between each metallic slab. This geometry is unrealistic experimentally but can be transformed by conformal mapping into tips or wedge-like structures [86–88], common in plasmonics, but also to finite nanostructures such as 2D open crescents [25–32] or overlapping nanowires [14, 18, 19] (see Sec.II C). The propagation of SPs along rough metal surfaces [89–91] can also be investigated through a conformal map of the structures shown in Fig.1(c)-(d).

B. *Perfect* singular structures

Our canonical system is a line dipole that can be located near a thin layer of metal (Fig.2(a)) or between two semi-infinite metal slabs (Fig.2(d)). In the following of the study, the metal permittivity is denoted as ϵ and the dielectric permittivity ϵ_d is

fixed arbitrarily to 1. Now apply the following CT:

$$z' = \frac{g^2}{z} \tag{5}$$

where $z = x + iy$ and $z' = x' + iy'$ are the usual complex number notations and g is an arbitrary length scale constant. Obviously all points at infinity in z translate to the origin in z' and planes translate into cylinders. Hence the resulting structures are a 2D crescent with touching tips (Fig.2(b)) and two kissing cylinders (Fig.2(e)).

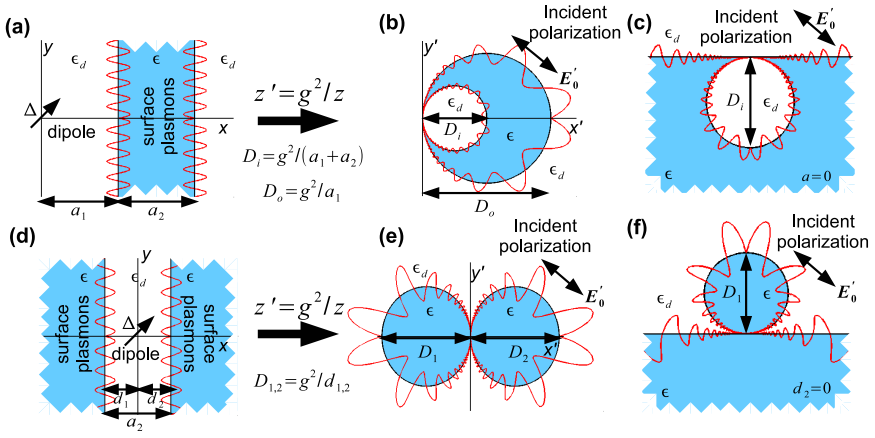

FIG. 2: (a) A thin layer of metal supports SPs that couple to a line dipole. (b) The latter structure is mapped onto a crescent-shaped nanowire illuminated by a uniform electric field following an inverse transformation of Eq.5. (c) If the dipole is placed on the metallic surface in the original frame ($a = 0$), the inversion map of Eq.5 leads to a semi-infinite metal slab with a hole drilled just below its surface. (d) Two semi-infinite metallic slabs separated by a thin dielectric film support SPs excited by a 2D dipole source. (e) The latter structure is mapped with Eq.5 onto two kissing nanowires illuminated by a uniform electric field. (f) If the dipole is placed at the surface of one of the metal plates in the initial geometry, the transformed structure is a nanowire placed just on top of a metal plate.

For the crescent, we define a key parameter ρ which is the ratio between the inner and outer diameters of the crescent, D_i and D_o respectively ($\rho = D_i/D_o$). Note that, if the line dipole is placed on the surface of the metal plate in the initial frames (Fig.2(a)-(d)), the resulting asymptotic structures are a cylindric hole drilled just below the surface of a metallic slab (Fig.2(e)) and a nanowire placed on top of a metal film (Fig.2(f)).

Transformation of the dipole is equally interesting - see Fig.2. We have chosen the origin of our inversion at the center of the dipole. Thus the two charges comprising the dipole, very close to the origin in z, translate to near infinity in z', which gives rise to a uniform electric field $\mathbf{E_0'}$ in the transformed geometry. To prove it more rigorously, one can first express the incident potential due to the dipole $\mathbf{\Delta} = \Delta_x \mathbf{u_x} + \Delta_y \mathbf{u_y}$ in the slab geometry,

$$\phi_{\mathbf{0}}(x,y) \;=\; -\frac{1}{2\pi\epsilon_0}\frac{\Delta_x x + \Delta_y y}{x^2+y^2} = -\frac{1}{2\pi\epsilon_0}\mathrm{Re}\left\{\frac{\overline{\Delta}}{z}\right\} \tag{6}$$

with $\overline{\Delta} = \Delta_x + i\Delta_y$ the complex notation applied to the dipole moment $\mathbf{\Delta}$. The incident potential is preserved under the CT ($\phi_0(z) = \phi_0'(z')$), which yields the following expression for the incident potential in the transformed geometry,

$$\phi_{\mathbf{0}}'(z') \;=\; -\frac{1}{2\pi\epsilon_0 g^2}\mathrm{Re}\left\{\overline{\Delta} z'\right\} \tag{7}$$

This incident potential can be related to a uniform electric field, $\mathbf{E_0'} = -\nabla\phi_0'$, such that

$$\mathbf{E_0'} = \frac{1}{2\pi\epsilon_0}\frac{\Delta_x \mathbf{u_x} - \Delta_y \mathbf{u_y}}{g^2}, \tag{8}$$

with $\mathbf{u_{x'}}$ and $\mathbf{u_{y'}}$ the unitary vectors along the axis (Ox') and (Oy'). This confirms our previous intuition that the dipole $\mathbf{\Delta}$ should map to a uniform electric field $\mathbf{E_0'}$. As we assume that the dimensions of the crescent and the kissing cylinders are small compared to the wavelength, the SP modes are well described in the near field approximation. The uniform electric field can then be taken as due to an incident plane wave of polarization $\mathbf{E_0'}$.

The mathematics of CT closely links the physics at work in each of the very different geometries. Solving the relatively tractable slab problems solves the crescent and kissing cylinders problems. In particular, the dispersion relation of the SP modes supported by IMI and MIM structures under the near-field approximation can be transposed to all the transformed geometries. The dispersion of the excitations can be derived from the following condition [70, 71]:

$$e^{2|k|a_2} - \left(\frac{\epsilon - 1}{\epsilon + 1}\right)^2 = 0 \tag{9}$$

The dispersion relation is thus given by,

$$ka_2 = \alpha = \begin{cases} \ln\left(\frac{\epsilon-1}{\epsilon+1}\right), & \text{if } \mathrm{Re}[\epsilon] < -1 \\ \ln\left(\frac{1-\epsilon}{\epsilon+1}\right), & \text{if } -1 < \mathrm{Re}[\epsilon] < 1 \end{cases} \tag{10}$$

with k the wavenumber of the SP modes. The dispersion relation is shown in Fig.3. The metal is assumed to be silver with a SP frequency $\omega_{sp} = 3.67$ eV and permittivity taken from Johnson and Christy [92]. The spectrum of modes is continuous

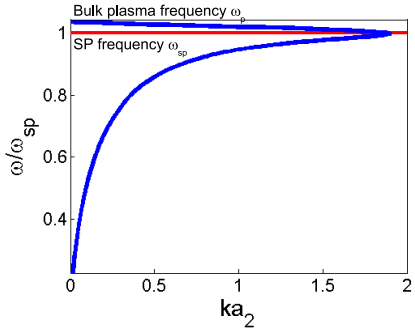

FIG. 3: Dispersion relation for IMI and MIM plasmonic structures shown in Fig.2(a) and (d).

with a lower bound at zero frequency and an upper bound at the bulk plasma frequency ω_p. At the SP frequency ω_{sp}, there is a singularity where the symmetry of the potential modes switches from antisymmetric to symmetric. Fig.3 indicate that the symmetric mode (namely, the SP excitation above the surface plasma frequency) is relatively narrow-band compared to the antisymmetric mode. Therefore, in the following of this review, we shall focus on the frequency range below the surface plasma frequency ω_{sp}.

In Fig.2(a)-(d), the dipole pumps energy into the SP modes of the metallic slab(s) which transport the energy out to infinity without reflection. The same modes are excited in the crescent and the kissing cylinders by the incident electric field $\mathbf{E}_0'$ (Eq.8). Since we make the near field approximation all dimensions are less than the wavelength but the changed geometry means that the excited modes have a net dipole moment. This provides coupling to the external field. Transformation of the modes tells us that in the crescent, modes are excited mainly at the fat part of the crescent and propagate around to the claws in an adiabatic fashion (Fig.2(c)). Similarly, the plasmon modes propagate along the surface of the kissing cylinders towards the touching point (Fig.2(e)). As SPs propagate towards the structure singularity, their wavelength shortens and velocity decreases in proportion. Just as modes excited in the original slab never reach infinity in a finite time, modes excited in the crescent or in kissing cylinders never reach the tips or the touching point. In an ideal lossless metal, energy accumulates towards the singularity, its density increasing with time without bound. In practice finite loss will resolve the situation leading to a balance between energy accumulation and dissipation. The harvesting and nanofocusing properties of the 2D crescent and kissing nanowires will be described in more details in Sec.III. The physics described until now is similar for the two asymptotic structures shown in Fig.2(c) and (f). The system consisting in a nanowire placed on top of a metal plate is investigated in details in Ref.[70].

Solving the 2D problem is interesting but quite restrictive in terms of applications. One can wonder if similar broadband and nanofocusing properties can be observed with 3D nanostructures like kissing spheres or a 3D crescent. This extension to 3D has been performed by A. Fernández-Domínguez *et al.*, using coordinate transformation [67]. Starting this time from the desired geometry, a dimer of kissing spheres (see Fig.4), the following 3D inversion can be applied

$$\mathbf{r}' = \frac{g^2}{|\mathbf{r}|^2}\mathbf{r} \tag{11}$$

where $\mathbf{r}$ and $\mathbf{r}'$ are the position vectors in the transformed and original space, respectively. Eq.11 transforms the spheres into two semi-infinite slabs. In contrast to 2D conformal mapping, the 3D inversion also acts on the material properties of the system.

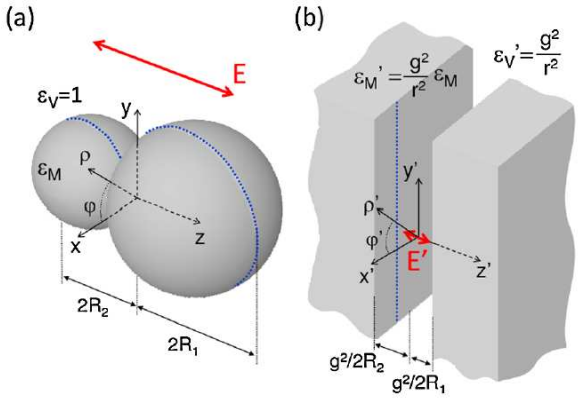

FIG. 4: Figure courtesy of Antonio Fernández-Domínguez [67]: Transformation used to solve the kissing spheres problem. (a) Two metal nanospheres of radii R_1 and R_2 touching at a single point. (b) Slab geometry with the illumination and permittivities obtained from the inversion of the kissing nanospheres.

TO determines that the transformed slabs are not filled with a conventional metal, but with a modified material having a spatially dependent dielectric function of the form $\epsilon'(r') = \epsilon g^2/r'^2$ and that the relative permittivity between them is $\epsilon'_v(r') = g^2/r'^2$. Fig.4(b) describes the geometry and the permittivity distribution obtained from the inversion of Fig.4(a).

Albeit more difficult to solve analytically, the 3D problem is actually very close to the 2D problem in terms of physics [67]. The SP propagate along the surface of the two kissing spheres towards the touching point. As they approach the structure singularity, their velocity decreases, which leads to an accumulation of energy. Actually, the nanofocusing performance is even better since the energy is focused onto a single point in 3D instead of a line in 2D. The system also displays a continuous spectrum with a lower bound at zero frequency and an upper bound at the bulk plasma frequency. The light absorption and nanofocusing properties of the kissing spheres will be described in more details in Sec.III C.

C. Singular plasmonic structures

1. *Conformal mapping of singular structures*

A more systematic study of singularities in plasmonics is now presented and relies on the work made by Y. Luo *et al.* [65]. The *mother* system is more complex than in the previous subsection (Fig.5(a) and (b)). It consists in an array of 2D dipoles located at $z = i2\pi md$ (with m an integer) embedded into a periodic stack of infinite metallic films. Each element of the dipole array is assumed to have a dipole moment $\mathbf{\Delta}$. The total incident field ϕ_0 is given by:

$$\phi_0(z) = -\frac{1}{2\pi\epsilon_0}\mathrm{Re}\left\{\sum_{m=-\infty}^{m=+\infty}\frac{\overline{\Delta}}{z - i2\pi md}\right\} \tag{12}$$

Now apply the following exponential transformation

$$w = d\exp\left(\frac{z}{d}\right) \tag{13}$$

where $w = u + iv$ is the complex number notation. This CT maps lines parallel to the $y-$axis of the original coordinate system to circles centered around the origin in the $w-$plane. A metallic wedge (Fig.5(c)) and a V-shaped metallic groove (Fig.5(d)) are thus obtained. A geometric singularity is created at the origin by the exponential map. The vertex angle of the wedge and the groove is denoted as θ. As to the transformation of the source, the conservation of the incident potential ($\phi_0(z) = \phi'_0(w)$) leads to:

$$\phi'_0(w) = -\frac{1}{2\pi\epsilon_0}\mathrm{Re}\left\{\sum_{m=-\infty}^{m=+\infty}\frac{\overline{\Delta}}{d\ln(w/d)}\right\} \tag{14}$$

Expanding the field about its singularity ($w = d$) leads to

$$\phi'_0(w) \;=\; -\frac{1}{2\pi\epsilon_0}\mathrm{Re}\left\{\frac{\overline{\Delta}}{w - d}\right\} \tag{15}$$

$$\tag{16}$$

Hence, the line dipole array is mapped to a single line dipole of same strength $\mathbf{\Delta}$ located at $w = d$.

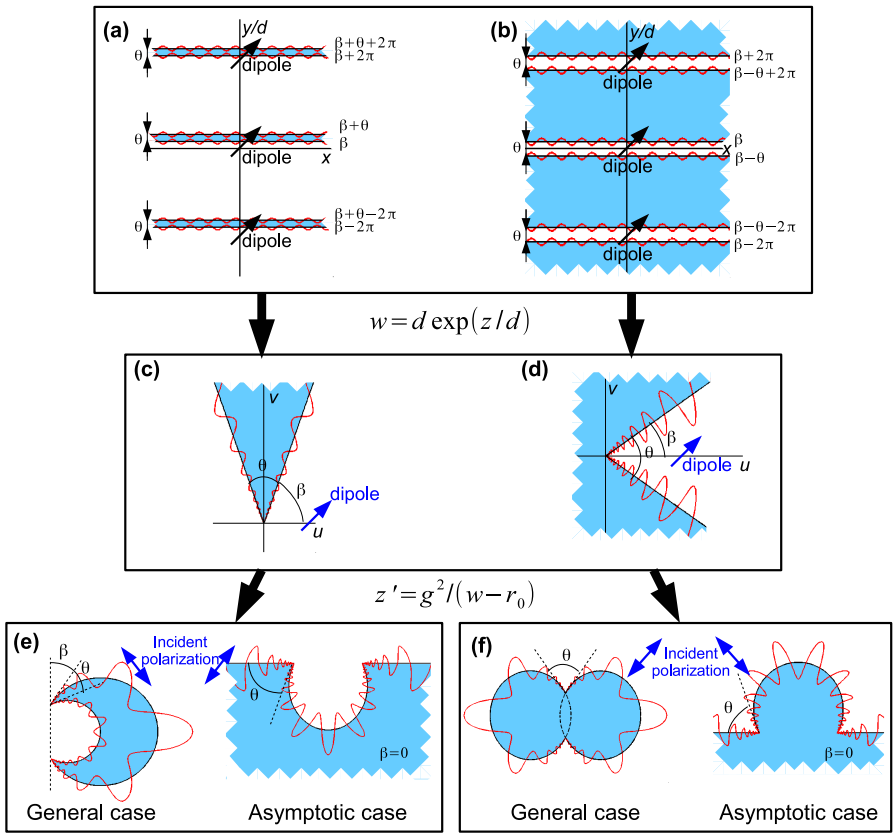

FIG. 5: (a),(b) Periodic metallic thin films support SPs that couple to a dipole array. The exponential map (Eq.13) transforms these two structures into a metallic wedge (c) and a V-shaped metallic groove (d). The array of dipoles is transformed into a single dipole of same strength $\mathbf{\Delta}$ located at $w = d$ (Eq.15). Finally, under the inversion mapping (Eq.17), the wedge/groove-like structures are converted to a metallic open crescent (e) and to overlapping nanowires (f). The dipole is mapped to a uniformed electric field $\mathbf{E}_0'$. In the particular case of a dipole placed along the metal wedge or groove, the transformed structures become a cylindrical groove engraved onto a metal surface (e) and a cylindrical protrusion partly embedded in a metal surface (f).

A new CT can be applied to the metallic groove and wedge. It consists in an inverse transformation about the dipole location:

$$z' = \frac{g^2}{w - d} \tag{17}$$

On the one hand, this transformation maps the groove to an open crescent-shaped structure in the general case and asymptotically to a cylindrical groove engraved onto a metal surface (convex rough surface, see Fig.5(e)). On the other hand, the inversion map of the wedge gives rise to overlapping nanowires in the general case and asymptotically to a cylindrical protrusion partly embedded in a metal surface (concave rough surface, see Fig.5(f)). In both cases, the dipole is transformed into a uniform electric field $\mathbf{E}_0'$ that we shall take as due to incident plane wave (Eq.8).

All the structures shown in Fig.5 share the same *DNA*. In particular, the singular structures derived in Fig.5(c)-(f) are characterized by the same vertex angle θ. Note that the *perfect* singular structures previously described in Sec.II B (Fig.2) constitute a particular case of the singular nanostructures under study with a vertex angle $\theta = 0$. The behavior of SPs in singular structures can be deduced from the *mother* systems (Figs.5(a)-(b)). In particular, the dispersion relation of the SP modes supported by the initial system can be transposed to all the transformed geometries. This dispersion relation is defined by the following equation [65]:

$$\left(\frac{\epsilon - 1}{\epsilon + 1}\right)^2 \left[e^{(2\pi-\theta)|k|d} - e^{\theta|k|d}\right]^2 - \left[e^{2\pi|k|d} - 1\right]^2 = 0 \tag{18}$$

Although, this relation is not tractable analytically, it can be solved recursively. The result is shown in Fig.6(a). The metal is still assumed to be silver [92]. The plasmonic system is shown to support a continuous spectrum of bounded SP modes with

symmetric and antisymmetric profiles of the tangential field E_x. The symmetric (or even) mode spans the frequency range $[\omega_c, \omega_{sp}]$, while the antisymmetric (or odd) mode spans the range $[\omega_{sp}, \omega_c']$. ω_c and ω_c' are the lower and upper bound cutoff frequencies determined by the following conditions:

$$\mathrm{Re}\{\epsilon(\omega_c)\} = \frac{\theta - 2\pi}{\theta},\ \mathrm{Re}\{\epsilon(\omega_c')\} = \frac{\theta}{\theta - 2\pi} \tag{19}$$

Although the dispersion relation cannot be solved analytically, two asymptotic solutions can be derived [73]:

$$kd\theta = \sqrt{\frac{3(\epsilon - \epsilon_c)}{\epsilon - \epsilon_c^3}},\ \text{for}\ \mathrm{Re}\{\epsilon\} \to \epsilon_c \tag{20}$$

$$kd\theta = \frac{1}{2}\ln\left(\frac{\epsilon - 1}{\epsilon + 1}\right),\ \text{for}\ \left|\ln\left(\frac{\epsilon - 1}{\epsilon + 1}\right)\right| >> -\epsilon_c^{-1} \tag{21}$$

These two asymptotes are superimposed to the dispersion relation in Fig.6(a).

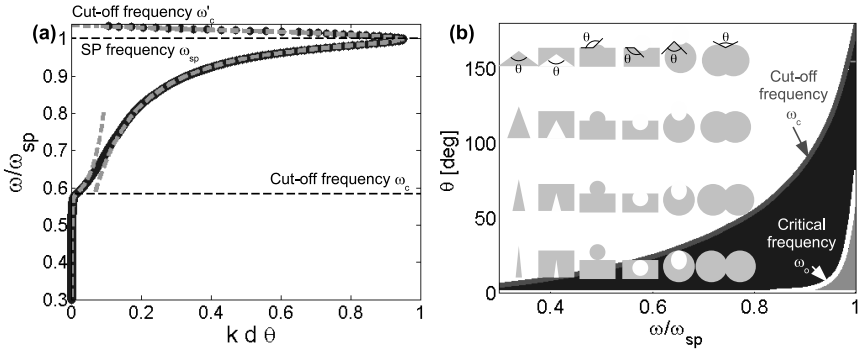

FIG. 6: (a) Dispersion relation of the SP modes supported by the plasmonic structures shown in Fig.5. (b) Evolution of the lower bound cut-off frequency ω_c (red line, Eq.19) and the critical frequency ω_0 (white line, Eq.36) as a function of the wavelength λ and of the vertex angle θ. The spectrum of SPs is continuous from ω_c to ω_{sp} (blue and light blue areas). The field is divergent at the singularity of the nanostructure for $\omega < \omega_0$ (blue area). For both panels, the metal is assumed to be silver [92].

The fact that all the plasmonic structures shown in Fig.5 share the same dispersion relation implies that they display the same broadband properties from ω_c to ω_c', as summarized in Fig.6(b). The bandwidth of these structures only depends on the vertex angle θ. The stronger the singularity is (*i.e* smaller theta), the broader the bandwidth of the light harvesting process is. As shown by Fig.5, they also share the same nanofocusing mechanism with an accumulation of energy about their geometrical singularity due to the distortion of the space under conformal mapping. The field is even divergent at the singularity below a certain critical frequency ω_0 that we will define in Sec.IV A (see Fig.6(b)). However, the nonlocal properties of ϵ encountered at small length scales will prevent the electric field from diverging at the singularity (see Sec.VII). Moreover, due to nanofabrication imperfections, the singularity of these structures cannot be perfectly reproduced in practice, which reduces the accumulation of energy at the tip of the singular structures.

2. Conformal mapping of blunt-ended singular structures

In this paragraph, the CT approach is applied to investigate the effect of the singularity bluntness on the harvesting and nanofocusing capabilities of singular nanostructures shown in Fig.5 [68]. To that aim, we will consider the example of blunted open crescents designed *via* conformal mapping as depicted in Fig.5(e).

Fig.7 shows the basic idea of the transformation strategy to deal with that issue. Compared to the original transformation shown in Fig.5, the blunt nanocrescent is simply obtained by blunting the sharp tips of the singular crescent structure (see Fig.7(b)). This change in the transformed frame implies a truncation of the infinite metallo-dielectric system on both sides in the initial frame (Fig.7(a)). The distances from the dipole to the two truncation points l_1 and l_2 determine, respectively, the bluntness of each tip of the crescent [68]

$$\delta_j = \frac{D\sin\beta\tan(\theta/2)}{|\sin_h[(l_j + i\beta)/2]\sin_h[(l_j + i\beta + i\theta)/2]|} \tag{22}$$

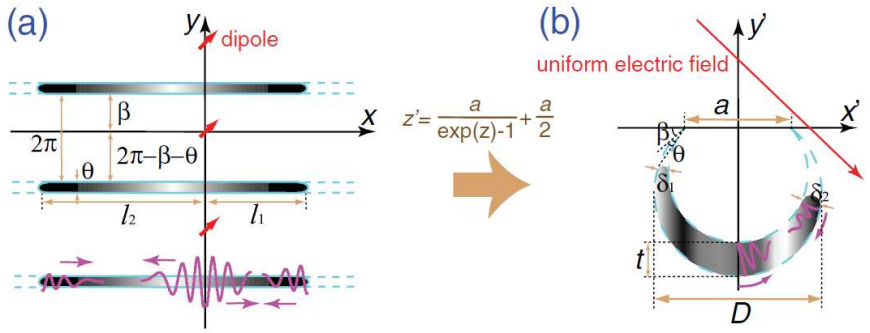

FIG. 7: Figure courtesy of Yu Luo [68]. The coordinate transformation which bridges (a) the truncated periodic metallodielectric system and (b) the blunt crescent. D is the total dimension of the crescent, a denotes the distance between the two crescent tips, t represents the maximum distance between the inner and outer crescent boundaries (referred to as the crescent thickness), θ is the vertex angle, and β denotes the angle between the x-axis and the outer boundary of the crescent.

δ_1 and δ_2 denote the bluntness dimensions (or the diameters at the two blunt tips). The remaining geometrical parameters D, θ, and β are defined in the figure caption of Fig.7.

Since the whole system under investigation has now a finite size along x, the SP modes are now distributed at several discrete spatial frequencies $k_n = n\pi/(l_1 + l_2)$, with n an integer. Replacing the continuous spatial frequency k by the discrete spatial frequencies k_n into the previous dispersion relation (Eq.18) leads to the following resonance condition,

$$\left(\frac{\epsilon-1}{\epsilon+1}\right)^2 \left[e^{nd\pi(2\pi-\theta)/(l_1+l_2)} - e^{nd\pi\theta/(l_1+l_2)}\right]^2 - \left[e^{2nd\pi^2/(l_1+l_2)} - 1\right]^2 = 0 \tag{23}$$

The bluntness imposed to the geometrical singularity makes the spectrum of modes become discrete. As shown in Ref.[68], the number of SP modes decreases exponentially as the tip bluntness increases. The SP modes are characterized by a linear momentum k_n in the original frame that maps onto an angular moment n in the transformed geometries. In Sec.IV B, we will show in more details the effect of the tip bluntness on the light harvesting and nanofocusing capabilities of singular nanostructures.

D. Resonant plasmonic structures

Until now, only singular structures have been studied within the CT approach. Resonant plasmonic structures are now considered since they do not rely on any geometrical singularity and thus will be easier to implement experimentally. To that aim, the initial geometry we consider are the MIM and IMI structures excited by an array of dipoles shown in Fig.8(a) and (b). Unlike in Sec.II B, the modes supported by these systems are discrete due to the presence of the dipole array and characterized by a linear momentum $k_n = 2\pi n/d$, with n an integer.

Now apply the exponential transformation already defined in Eq.13. The IMI structure (Fig.8(a)) leads to a metallic nanotube (see Fig.8(c)), whereas the MIM structure (Fig.8(b)) gives rise to the complementary structure, *i.e* an insulator nanotube drilled into a block of metal (see Fig.8(d)). The transformation of the source is the same as before: the array of dipoles $\mathbf{\Delta}$ maps into a single dipole $\mathbf{\Delta}$ located at $w = d$ (Eq.15). The linear momentum of the SP modes supported by the original systems now map to the angular momentum of SPs that propagate along the insulator-metal surfaces. The configurations described in Fig.8(c)-(d) can correspond to the experimental situation of a molecule of transition dipole moment $\mathbf{\Delta}$ interacting with LSPs supported by a nanotube [93, 94], but we can go beyond these simple configurations by applying a new inverse transformation at the dipole position (Eq.17). On the one hand, the metallic tube (Fig.8(c)) is transformed into an off-axis nanotube in the general case and asymptotically to a hole drilled below the surface of a metal plate (Fig.8(e)). On the other hand, the insulator tube (Fig.8(d)) maps to a dimer of nanowires in the general case and asymptotically to a nanowire on top of a metal plate separated by a thin layer of insulator (Fig.8(f)). Once again, the dipole of Fig.8(c)-(d) maps to an incident plane wave $\mathbf{E_0'}$ (Eq.8).

As their *mother* system, the new structures display a discrete spectrum of modes $k_n = 2\pi n/d$, in agreement with the hybridization picture [15, 36]. Replacing the continuous spatial frequency k by k_n into Eq.9 leads to the following resonance condition,

$$\exp\left(\frac{4\pi n a_2}{d}\right) = \left(\frac{\epsilon-1}{\epsilon+1}\right)^2 \tag{24}$$

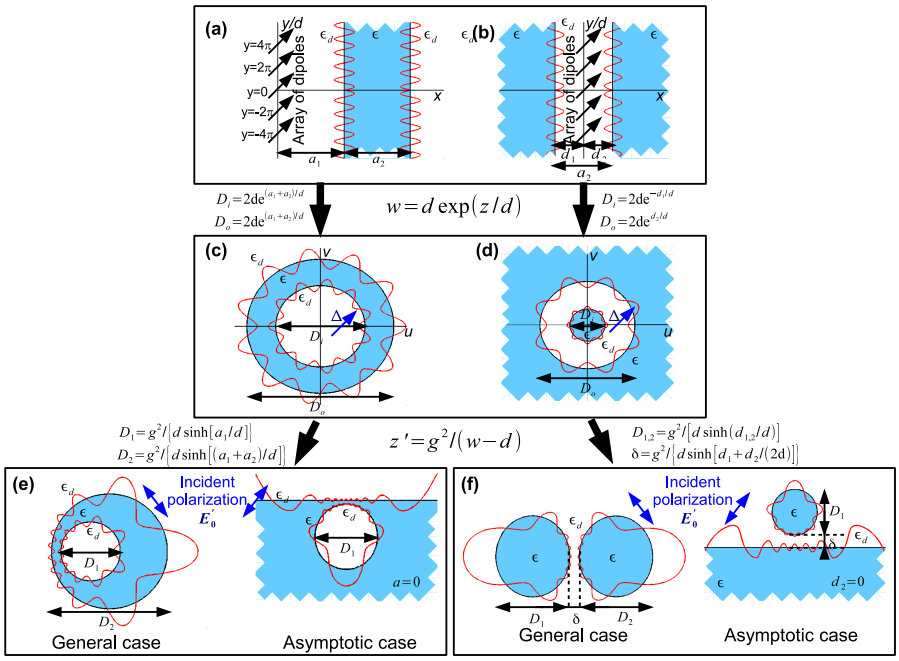

FIG. 8: An array of dipoles $\mathbf{\Delta}$ with a pitch $2\pi d$ excites the SP modes supported by an IMI (a) and MIM (b) structure. Upon exponential mapping (Eq.13), these two materials are transformed into a metallic nanotube (c) and its complementary structure (d) excited by a single dipole of same strength $\mathbf{\Delta}$. Finally, an inverse transformation of (c) and (d) about the dipole location (Eq.17) leads to a nanotube (e) and a dimer of nanowires (f) illuminated by a uniform electric field $\mathbf{E_0'}$. When the dipole is placed at the metal surface in (c) and (d), these two structures become asymptotically an insulator hole drilled into a semi-infinite metal plate (e) and a nanowire placed on top of a metal plate with a thin layer of insulator between them (f).

This resonance condition can be rewritten for the transformed geometry. For instance, it yields for a dimer with nanowires of equal diameter ($D = D_1 = D_2$) [66, 74],

$$\left(\sqrt{\rho'} + \sqrt{1+\rho'}\right)^{4n} = \mathrm{Re}\left\{\frac{\epsilon - 1}{\epsilon + 1}\right\} \tag{25}$$

Note that this condition of resonance only depends on the ratio $\rho' = \delta/(2D)$ between the gap δ and the overall physical cross-section $2D$. Each mode may give rise to a resonance which is red-shifted when the two nanowires approach each other, as it will be shown in Sec.V. The transformation shown in Fig.8 tells us that these modes couple to each other in the narrow gap separating the two nanowires (Fig.8(f)) or when the nanotube gets thinner (Fig.8(e)): their wavelength and velocity decrease, leading to an important field enhancement at this location. However, contrary to the kissing cylinders or the crescent-shaped cylinder (see Sec.II B), their velocity does not vanish, hence the LSPs turn infinitely around the nanoparticles before being absorbed. This accounts for their resonant behavior. This brief qualitative account will be completed by quantitative results in Sec.V.

This section has presented the three main families of nanostructures that can be derived by conformal mapping from the classical MIM and IMI structures (Fig.1). In the three next sections, we will present the main analytical results provided by this CT approach for each of these families.

III. BROADBAND LIGHT HARVESTING AND NANOFOCUSING

This section deals with the light harvesting and nanofocusing properties of touching dimers and crescents-shaped nanostructures (see Fig.2). It reviews the main results presented in a series of three papers [45, 70, 71].

A. Broadband light absorption

The absorption cross-section of nanostructures can be directly derived from the dipole power dissipated in the initial frame [70, 71]. The energy pumped into the SPs in the metal slab(s) (Fig.2(a)) can be calculated from the scalar product of the induced

electric field and the dipole [95]:

$$P = -\frac{\omega}{2}\,\mathrm{Im}\left\{\mathbf{\Delta}^{*}.\mathbf{E}(z=0)\right\} \tag{26}$$

This quantity can be calculated in the near field approximation by picking out the poles due to the propagating SP modes [70, 71]. This dipole power dissipated maps directly onto the power absorbed from a plane wave incident on the nanostructure in the transformed geometry. Following this strategy, the absorption cross-section σ_a of the crescent can be deduced for $\epsilon < -1$ [71]

$$\sigma_a = \frac{\pi^2\omega}{c}\left[\frac{\rho D_o}{1-\rho}\right]^2 \mathrm{Re}\left\{\ln\left(\frac{\epsilon-1}{\epsilon+1}\right)\frac{4\epsilon}{1-\epsilon^2}\left(\frac{\epsilon-1}{\epsilon+1}\right)^{-\frac{2\rho}{1-\rho}}\right\} \tag{27}$$

Note that all orientations of the incident electric field are equally effective at excitation. This isotropy is allowed by the contact between the two crescent tips. On the contrary, an highly anisotropic behavior is expected as soon as the tips are no longer touching [26–29, 65]. At the surface plasma frequency where $\epsilon = -1$, Eq.27 is singular if $\rho = D_i/D_o < 1/3$, *i.e* only for fat crescents. Fig.9(a) and (b) display the wave-length dependence absorption cross-section σ_a as a fraction of the physical cross-section, for $D_o = 20$ nm and considering silver [92]. For $\rho > 1/3$, the crescent exhibits a broadband spectrum that shifts towards red when the crescent gets thinner. The efficiency of the crescent in light harvesting is also significant since its absorption cross-section is of the order of the physical cross-section even for such a small particle size ($D_o = 20$ nm).

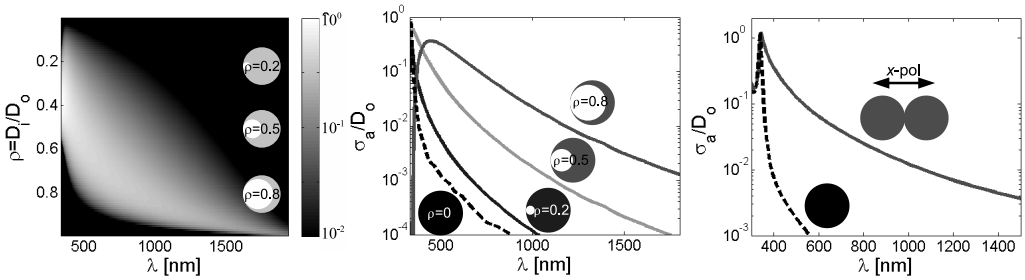

FIG. 9: (a) Absorption cross-section of the 2D crescent as a fraction of the physical cross-section as a function of ρ and the wavelength. (b) The same result is shown for ρ =0.2, 0.5, 0.8 and compared to the case of a single nanowire [96]. (c) Absorption cross-section of the kissing cylinders as a fraction of the physical cross-section $D_o = 2D$ as a function of the wavelength λ for an incident electric field polarized along x'. The overall size D_o of each device is 20 nm. All the graphs are shown in log-scale.

The same analytical calculation can be performed for two kissing nanowires of same diameter ($D = D_1 = D_2$). However, unlike the crescent, this plasmonic device is strongly dependent on the polarization of the incoming field. Indeed, the two kissing cylinders geometry is derived from a MIM plasmonic structure (Fig.2(d)). This configuration only supports odd SP modes for $\epsilon < -1$ [70]. If the dipole is placed at the center of the two metal slabs, only its $x-$component can give rise to odd SP modes and its $y-$component is totally ineffective. In the transformed geometry, it means that only the $x'-$component of the incident electric field can excite SPs for two kissing cylinders of the same diameter. The corresponding absorption cross-section σ_a can be derived for $\epsilon < -1$ [70]

$$\sigma_a = \frac{\pi^2\omega}{c}D^2\ \mathrm{Re}\left\{\ln\left(\frac{\epsilon-1}{\epsilon+1}\right)\right\} \tag{28}$$

Fig.9(c) displays σ_a as a fraction of the physical cross-section ($D_o = 2D = 20$ nm). Similarly to the crescent, the two kissing cylinders are powerful light harvesting devices over a broadband spectrum for an incident wave polarized along x'. Note that, in both cases, σ_a/D scales linearly with D. Thus higher cross-sections could be obtained for larger dimension but in this case our near field analytic theory may not be valid [45, 72] (see Sec.VI B).

B. Balance between energy accumulation and dissipation

The 2D crescent and kissing nanowires are capable of an efficient harvesting of light over the visible and near infrared spectra. As we will see now, they are also strong far-field to near-field converters of energy, providing a considerable confinement and amplification of the electric field in the vicinity of their physical singularity. Fig.10(a) and (b) illustrate this fact by showing our analytical calculation of the field distribution in the two nanostructures. The metal is still silver [92]. In the slab frame, the SP modes transport the energy of the dipole out to infinity (see Fig.2). In the transformed frame, the same modes are excited in the

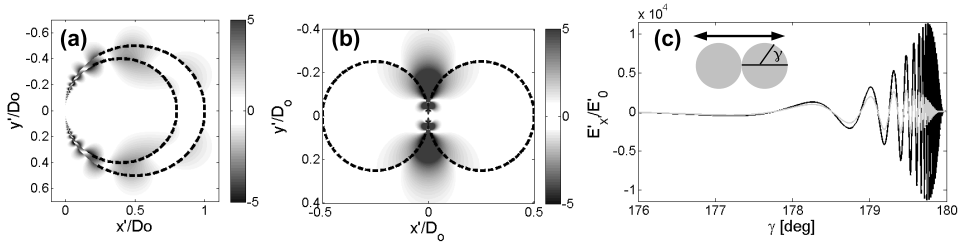

FIG. 10: Amplitude of the x'-component of the electric field normalized by the incoming field (polarized along x'). The (a) and (b) panels display the field in the crescent (for $\rho = 0.8$) and in the two kissing cylinders respectively, considering silver at $\omega = 0.9\omega_{sp}$. The color scale is restricted to [-5 5] but note that the field magnitude is by far larger around the singularity of the structures. (c) The electric field is plotted along the surface of the kissing nanowires, plotted as a function of the angle, γ, defined in the figure, for $\omega = 0.75\omega_{sp}$, $\epsilon = -7.06 + 0.21i$ [92] (blue curve) and $\epsilon = -7.06 + 2 \times 0.21i$ (red curve, losses $\times 2$). Both curves are normalized to the incoming field amplitude E'_0.

fat part of the crescent and the diametrically opposite sides of the kissing cylinders. Then, they propagate around the claws of the crescent and the surface of nanowires in an adiabatic fashion.

Fig.10(c) shows our analytic calculation of the electric field induced at the surface of the kissing cylinders by a plane wave polarized along the x' axis. As pointed out previously, the wavelength of SPPs shortens as they approach the touching point, leading to an enhancement of the electric field. The growth of the field is then truncated by absorption losses at a finite angle. A total field enhancement of 2×10^3 arises here at an angle $\theta = 179.75\,\mathrm{deg}$. Also shown is a second calculation in which losses are increased by a factor of two greatly reducing the enhancement, and decreasing the angle at which maximum enhancement occurs.

For kissing nanowires, the field enhancement $|E'|/E'_{0x}$ along the nanowire can be expressed, for $\epsilon < -1$, as [70]

$$\left|\frac{E'}{E'_{0x}}\right| \;=\; \frac{\pi}{2}|\alpha|\,|\cosh(\alpha)|^{1/2}\,\frac{\exp\left(-\mathrm{Im}\{\gamma\}|\tan(\gamma/2)|/2\right)}{\cos^2(\gamma/2)} \tag{29}$$

with γ, the angle defined in the inset of Fig.10(c), and α defined in Eq.10. The exponential term of the last equation shows how the dissipation losses truncate the growth of the field along the cylinders surface. From this expression of $|E'|/E'_{0x}$ and using the fact that $\mathrm{Im}\{\alpha\} = \mathrm{atan}(2\epsilon_I/(|\epsilon|^2 - 1))$, the angle γ_{max} at which the maximum field enhancement occurs can be easily deduced as a function of the permittivity imaginary part ϵ_I [70],

$$\gamma_{max} \simeq \pi - \frac{2(1-\rho)\epsilon_I}{|\epsilon|^2 - 1}, \text{ if } \epsilon_I << |\epsilon|^2 - 1 \tag{30}$$

This expression of γ_{max} shows that an increase of the dissipation losses makes the maximum field enhancement shift to smaller angles, resulting in a worse confinement of the field around the structure singularity.

By injecting the expression of γ_{max} (Eq.30) into Eq.29 and replacing α by its expression (Eq.10), one can deduce the maximum field enhancement, $|E'_{max}|/E'_{0x}$, that can be expected at the surface of the kissing cylinders, for $\epsilon_I << |\epsilon|^2 - 1$ [70],

$$\left|\frac{E'_{max}}{E'_{0x}}\right| \;\simeq\; \frac{2\pi}{e^2}\left|\ln\left(\frac{\epsilon-1}{\epsilon+1}\right)\sqrt{\frac{\epsilon^2+1}{\epsilon^2-1}}\right|\frac{(|\epsilon|^2-1)^2}{\epsilon_I^2} \tag{31}$$

The dissipation losses reduce the field enhancement as the inverse square of the permittivity imaginary part ϵ_I. This explains the ratio 4 observed between the blue and red curves in Fig.10(c). The same analytic calculations can be performed for the crescent [71] or for a nanowire placed on top of a metal plate [70] (Fig.2(f)).

Note that the field enhancement displayed by Fig.10(c) may be unrealistic in practice. There are indeed two limits to the CT approach:

- A micro-scale limit: when the size of the device becomes comparable with the wave length, radiation losses are non longer negligible and will reduce the field enhancement induced by the nanostructure. This point has been addressed for kissing nanowires in Ref.[72] and will be discussed in this review in Sec.VI B for the case of a dimer of non-touching nanowires.

- A nano-scale limit: at small length scales, continuum electrodynamics is no longer valid and non-local effects can result in an increase of the permittivity imaginary part [4, 97–100]. This issue will be addressed in Sec.VII. Furthermore, quantum mechanical effects, such as electron tunnelling or screening, have to be taken into account in the vicinity of the structure singularity and may also reduce the field enhancement relative to classical predictions [101].

C. Extension to 3D

In Sec.II B, we have shown how the 2D conformal mapping of kissing nanowires can be extended to 3D leading to the study of the kissing spheres (Fig.4). The problem cannot be solved exactly due to the spatial variations of the permittivity in the slab frame, but describe accurately the EM fields behavior at the touching point of the spheres. A quite simple expression can be found for the absorption cross-section of two identical kissing spheres of radii R_1 with an incident polarization along x' [67]

$$\sigma_a = \frac{64\pi^2}{3}\frac{\omega}{c}R_1^3 \mathrm{Re}\left\{\alpha^2 - \alpha\right\} \tag{32}$$

Fig.11(a) plots the absorption cross-section σ_a normalized by R_1^3 for kissing spheres of different dimensions calculated using COMSOL multiphysics (color or shaded dots). The metal is assumed to be silver with a permittivity taken from Palik [102]. The analytical spectrum obtained from Eq.32 is also shown in black solid line. The agreement between theory and simulations is remarkable for radii up to 35 nm, where the near-field approximation fails and radiation losses become significant. Note that the comparison for small R_1 worsens at high frequencies, as metal absorption prevents EM fields from reaching the touching point, where the theoretical result is the most accurate. Fig.11(a) indicates that σ_a for small dimers is of the order of the physical size even at frequencies well below the single sphere resonance (black dots). This demonstrates that touching dimers strongly interact with radiation over the whole optical spectrum, and that their cross-section presents a much smoother dependence on frequency than an isolated nanoparticle.

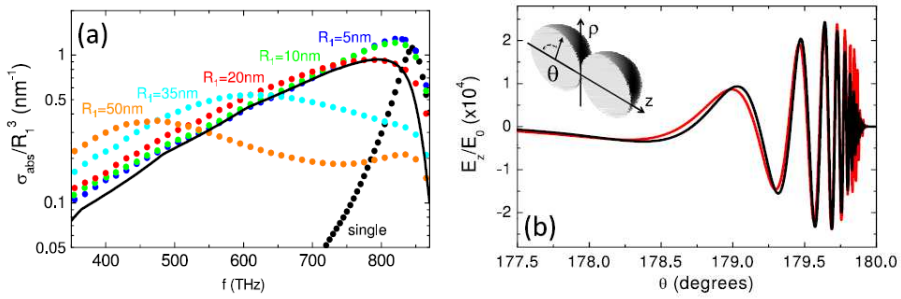

FIG. 11: Figure courtesy of Antonio Fernández-Domínguez [67]. (a) Numerical absorption cross section σ_a versus incident frequency for twin Ag touching spheres of different radii R_1 (color or shaded dots), and a single 5 nm radius sphere (black dots). Black solid line plots the analytical result obtained from Eq.32. All the spectra are normalized to R_1^3. (b) Electric field amplitude enhancement versus angle θ (defined in the inset) at 500 THz ($R_1 = 20$ nm). Black (red or gray) line corresponds to analytical (numerical) calculations (Eq.33).

In order to gain a physical insight into the origin of the broadband response of touching spheres, the amplitude enhancement of the $z-$component of the electric field close to the contact point is plotted in Fig.11(b). Fields are evaluated at 600 nm (500 THz, $\epsilon = -16.0 + 2.1i$), where the dimer cross section is 50 times larger than the single sphere. For this magnitude, the TO approach yields [67]

$$\frac{E'_z}{E'_0} = \frac{\pi}{\sqrt{2}(1+\cos\theta)^{3/2}}\mathrm{Re}\left\{\alpha^2(3e^{\alpha/2}+e^{-\alpha/2})J_0\left(\frac{\alpha}{2}\frac{\sin\theta}{1+\cos\theta}\right)\right\} \tag{33}$$

where θ is defined in the inset of Fig.11(b) and J_0 is the Bessel function of rank 0. There is again a good agreement between theory (black) and simulations (red) for spheres of radius 20 nm. E'_z/E'_0 is superior to 10^4 at the vicinity of the contact point of the spheres far from the single particle resonance. This is a clear demonstration of the broadband superfocusing capabilities of the structure. The physics is similar to the 2D case: energy accumulates due to the drastic reduction of group velocity and effective wavelength that the surface waves experience while approaching the contact point of the dimer. Note that neither the TO model nor the numerical simulations include nonlocal effects (see Sec.VII).

D. Conclusion

This section has highlighted the power and elegance of the CT approach. On the one hand, this approach allows to design a path towards a broadband nanofocusing of light at the nanoscale. On the other hand, it provides novel insights on the physical behavior of SPs at the nanoscale. The nanostructures derived from conformal mapping should rely on perfectly shaped singularities on which drastic hot spots arise. In practice, such a geometry will be particularly difficult to implement. In the next section, this issue is addressed by considering the bluntness of plasmonic structures at the nanoscale, considering the conformal map described in Sec.II C 2.

IV. SURFACE PLASMONS AND SINGULARITIES

This section deals with the light harvesting and nanofocusing properties provided by the family of nanostructures described in Fig.5 (V-groove, wedge, open crescent, rough surface, overlapping nanowires). These nanotructures have been studied in details in a series of paper [65, 73, 75]. Here we will first focus on the effect of the vertex angle on the bandwidth of the light harvesting properties by considering the example of overlapping nanowires [73]. Second, we will show how conformal mapping can address the issue of not perfectly shaped singularities [68], inherent in any nanofabrication process.

A. Control of the bandwidth with the vertex angle

The last section has addressed the issue of singular nanostructures (crescent, kissing nanowires) whose singularity are characterized by a zero vertex angle. This situation is quite irrealistic experimentally, hence one can wonder what happens when the vertex angle θ increases. Here, we will study the transition between kissing nanowires studied in Sec.III and overlapping nanowires (Fig.5(f)) that has been studied in details by D. Y. Lei *et al.* [73].

Solving the problem in the slab frame allows to derive the absorption cross-section σ_a following the same strategy as the one described in Sec.III A. A full-analytical expression of σ_a for two overlapping nanowires of same diameter D is not available but one can derive the following asymptotic limits for an incident wave polarized along x' [73]

$$\sigma_a \sim 4\pi^2\sqrt{3}\frac{\omega}{c}\frac{\sin^2(\theta/2)}{\theta^2}D^2\mathrm{Re}\left\{\sqrt{\frac{\epsilon_c}{1-\epsilon_c^2}}\frac{1}{\sqrt{\epsilon-\epsilon_c}}\right\},\ \text{if Re}\{\epsilon\}\rightarrow\epsilon_c \tag{34}$$

$$\sigma_a \sim 4\pi^2\frac{\omega}{c}\frac{\sin^2(\theta/2)}{\theta^2}D^2\mathrm{Re}\left\{\ln\left(\frac{\epsilon-1}{\epsilon+1}\right)\right\},\ \text{if}\ \left|\ln\left(\frac{\epsilon-1}{\epsilon+1}\right)\right| >> -\epsilon_c^{-1} \tag{35}$$

with ϵ_c, the permittivity threshold defined in Eq.19. The first asymptote of σ_a (Eq. 34) displays a square-root singularity at the cut-off frequency ω_c, for which $\mathrm{Re}\{\epsilon\}=\epsilon_c$. The second asymptote (Eq. 35) applies for larger frequencies than ω_c and is strictly identical to the expression derived for kissing cylinders (Eq.28). Fig.12(a) displays the absorption cross-section of overlapping nanowires normalized by the overall physical cross-section D_o as a function of the wavelength λ and the vertex angle θ. Fig.12(b) displays the wavelength dependence of σ_a for different values of the vertex angle θ. The two asymptotes derived in Eqs.34 and 35 are superimposed to σ_a. As shown in Fig.12, the absorption spectrum is strongly dependent on the

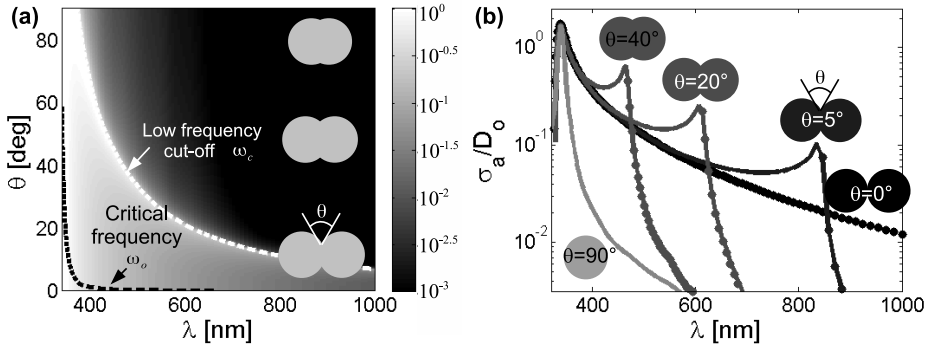

FIG. 12: (a) Absorption cross-section σ_a normalized by the physical cross-section D_o as a function of θ and λ for an overlapping cylinders pair of overall size $D_o = 20$ nm. The white dashed line represents the low-frequency cut-off ω_c. The white continuous line represents the frequency ω_o (Eq.36). The color bar is in log-scale. (b) The same quantity is displayed as a function of frequency for different values of $\theta = 5^o$ (blue), 20^o (green), 40^o (red). The low-frequency asymptotes (coloured dots, Eq.34) and the high-frequency asymptote (black dots, Eq.35) are shown. At last, the single cylinder case is also shown for comparison [96] (cyan continuous line). For both panels, the metal is silver [92]

vertex angle θ, which governs the cut-off frequency ω_c (Eq.19). Three distinct regimes can be distinguished:

- Kissing cylinders regime ($\theta \rightarrow 0^o$): The absorption spectrum of kissing nanowires corresponds to the high-frequency asymptote derived in Eq.35 (see Fig.12(b)). In that case, the cut-off frequency ω_c is zero and the absorption cross-section displays a continuous and broadband absorption spectrum over the whole visible and near-infrared spectra.
- Overlapping regime ($0^o < \theta < 90^o$): When the vertex angle θ increases, the cut-off frequency ω_c blue-shifts, which limits the bandwidth of the light harvesting process. An absorption peak is observed around ω_c and its line shape is well predicted by Eq.34 for $\omega < \omega_c$. When $\omega \rightarrow \omega_{sp}$, the device behaves like kissing cylinders (Eq.35) in terms of light harvesting (see Fig.12(b)). The comparison stops here since the nanofocusing behaviors differ in both situations.

- Single nanowire regime ($\theta \rightarrow 90^o$): the two nanowires merge into a single one. The absorption spectrum exhibits one sharp resonance at the SP frequency ω_{sp} (see Fig.12(b)).

In contrast to kissing nanowires, overlapping nanowires show a clear cut-off frequency ω_c in their absorption spectrum. This cut-off frequency can be adjusted by tailoring the overlap distance between the two nanowires. Note that the spectral properties shown by overlapping nanowires can be extended to all the structures displayed in Fig.5: A squeezed metallic wedge $\theta \rightarrow 0^o$ can support SP modes over a broad bandwidth, whereas large angles $\theta \rightarrow 90^o$ imply an extremely narrow line width.

The nanofocusing mechanism is on the contrary quite different compared to kissing nanowires (see Sec.III). The field can be actually divergent at the singularity for the family of nanostructures shown in Fig.5. The field divergence condition can be rewritten as [65, 73]

$$\arctan\left[\frac{2\mathrm{Im}\{\epsilon\}}{|\epsilon|^2+1}\right] < \theta \tag{36}$$

The term on the left is directly related to the dissipation losses in the metal with the imaginary part of the permittivity. The term on the right is the vertex angle which accounts for the field compression at the structure singularities. Let us introduce ω_0 the frequency for which the two terms of the last equation are equal. Below ω_0, Eq.36 is checked: the field compression dominates over dissipation losses and the field diverges at the structure singularities. Beyond ω_0, Eq.36 is no longer verified: the dissipation losses are large enough to make the field vanish at the structure singularity. The wavelengths corresponding to ω_0 and ω_c are shown as a function of θ and are superimposed to the absorption spectrum in Fig.12(a). The comparison between the two curves shows that the frequency ω_0 is clearly larger than the cutoff frequency ω_c and that both frequencies blue-shift with the overlap distance. The divergence of the electric field occurs over most of the overlapping nanowires bandwidth. This divergent behavior is surprising but not realistic in practice since it is strongly dependent on how sharp the singularity is.

B. Effect of the bluntness

The effect of bluntness on singular nanostructures is now investigated considering the example of blunt-ended nanocrescents (see Fig.7). However, note that this strategy can be applied to the whole set of singular plasmonic structures displayed in Figs.2 and 5. The absorption cross section σ_a of the crescent can be directly deduced from the power dissipated by the dipole in the original frame shown in Fig.7(a). Analytical details are presented in Ref.[68]. Fig.13(a) shows the evolution of the absorption spectrum as a function of the bluntness δ of the tip crescent (Eq.22). Three distinct regimes can be distinguished:

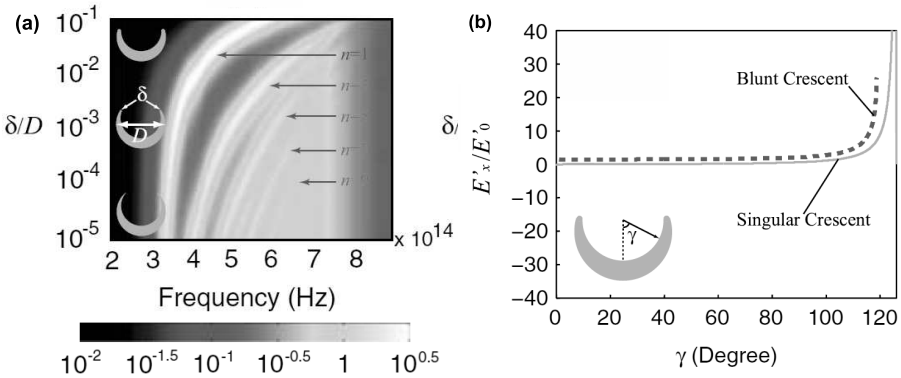

FIG. 13: Figure courtesy of Yu Luo [68] (a) Normalized absorption cross sections σ/D as a function of frequency and the tip bluntness δ for a nanocrescent with $\theta = 9^o$ and $t = 0.16D$. (b) Normalized electric fields $E'_{x'}/E'_0$ along the inner boundaries of the blunt and the corresponding singular crescents at $f = 368THz$ (the resonance of the dipole mode ω_c). Here, the geometry parameters are set as $\theta = 9^o$, $t = 0.16D$ and $\delta = 0.01D$ (for the blunt crescent). The metal is silver considering Palik data [102].

- Single-resonance structure ($\delta/D > 10^{-1}$): the absorption spectrum displays only one sharp resonance at ω_{sp}. The system behaves like a single rounded nanoparticle.
- Multi-resonance regime ($0 < \delta/D < 10^{-1}$): When the tips of the nanocrescent become sharper, resonances associated to a small angular moment n start to arise at a smaller frequency than ω_{sp}. These resonances are red-shifted when δ decreases and the absorption spectrum displays several resonances in the visible spectrum in addition to the overall structure resonance at ω_{sp}.

- Broadband regime ($\delta/D \to 0$): When the tips become extremely sharp, the absorption spectrum becomes continuous and broadband with a lower cut-off frequency ω_c depending only on the vertex angle θ.

Fig.13(a) indicates the degree of sharpness required to obtain a broadband harvesting of light. In the conditions of Fig.13(a) ($\theta = 9^o$, $t = 0.16D$), a bluntness $\delta/D = 10^{-2}$ is sufficient to get an efficient light absorption from $f = 350$ THz ($\lambda = 850$ nm) to $f = 900$ THz ($\lambda = 333$ nm), *i.e* over the whole visible spectrum.

Fig.13(b) shows the effect of the bluntness on the field enhancement that arise in the vicinity of the singularity. The normalized electric field $E'_{x'}/E'_0$ is plotted along the inner boundaries as a function of the angle γ defined in the inset. The case of the blunt (red dashed line) and the corresponding singular (blue solid line) crescents are compared. As expected, the maximum field enhancement is distinctly decreased around 25 as the claw tips are rounded. However, away from the tip, the field only undergoes minor changes due to the bluntness. It should be pointed out that quantum mechanical effects are not considered in our calculation. For subnanometer bluntness dimensions, a more general quantum description and nonlocal constitutive relation of the metal may be necessary to further improve the analytical model [15, 97].

V. PLASMONIC HYBRIDIZATION REVISITED WITH TRANSFORMATION OPTICS

This section deals with the light harvesting and nanofocusing properties provided by the family of resonant nanostructures described in Fig.8 (metallic nanotubes, nanowire dimer, *etc.*). Such nanotructures have been widely studied both theoretically, numerically and experimentally in the literature [10, 11, 13, 15, 17, 18, 20, 33–39, 83–85]. An elegant physical picture to describe these resonant structures is the plasmon hybridization model [15, 36]. In analogy with molecular orbital theory, the dimer plasmons can be viewed as bonding and antibonding combinations of the individual nanoparticle plasmons. However, albeit elegant, the plasmon hybridization picture is a limited tool: numerical simulations are still needed to calculate the optical response of the nanostructures. On the contrary, the CT approach provides an analytical description of the plasmonic hybridization and a unique physical insight on the propagation of SPs in that kind of nanostructures [66, 74].

A. A resonant behavior

In this section, we will consider the example of a dimer of nanowires [66, 74] to illustrate the plasmonic hybridization concept. However, note that the same strategy can be applied to solve the problem of off-axis nanotubes (Fig.8(e)).

The absorption cross-section σ_a of a cylinder pair (Fig.8(f)) can be deduced in the quasi-static limit from the power absorbed by each dipole in the original frame (Fig.8(b)). The following expression of σ_a is found for an incident wave polarized along x' [66]

$$\sigma_a = \mathrm{Im}\left\{16\pi\frac{\omega}{c}\rho'(1+\rho')D^2\chi\right\} \tag{37}$$

$$\text{with, } \chi = \frac{\epsilon-1}{\epsilon+1}\sum_{n=1}^{+\infty}\frac{n}{\left[\sqrt{\rho'}+\sqrt{1+\rho'}\right]^{4n} - \frac{\epsilon-1}{\epsilon+1}} \tag{38}$$

with ρ' the ratio between the gap δ between the two nanowires and $2D$ their added diameters. The parameter χ in Eq.38 displays the sum of each contribution due to the LSP modes supported by the cylinder pair and denoted by their angular moment n. Each mode may give rise to a resonance at a frequency satisfying the condition previously defined in Eq.25.

Fig.14 illustrates this resonant feature by displaying $\sigma_a/(2D)$ as a function of frequency and $\rho' = \delta/2D$, for an overall physical cross-section $2D = 20$ nm. The metal is silver with a permittivity taken from Johnson and Christy [92]. As shown by Fig.14, the absorption spectrum is strongly dependent on the ratio $\rho' = \delta/(2D)$ and let show three distinct regimes:

- Weak coupling regime ($\rho' > 0.5$, i.e for a gap larger than the cylinder diameter): all the modes resonate at the vicinity of the surface plasma frequency ω_{sp}. The coupling between the two nanoparticles is weak and the system exhibits the same absorption spectrum as an individual cylinder.

- Strong coupling regime ($\rho' < 0.5$): when the two nanoparticles are approached by less than one diameter, resonances for small n start to arise at a smaller frequency than ω_{sp}. These resonances are red shifted when the gap decreases and the absorption spectrum displays several resonances in the visible spectrum in addition to the individual LSPs resonance at ω_{sp}.

- Kissing cylinders regime ($\rho' \to 0$): the number of excited modes becomes infinite, leading to a continuous and broadband absorption spectrum (Fig.9(c)).

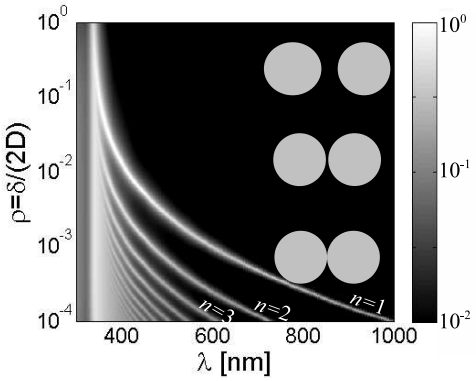

FIG. 14: Absorption cross-section σ_{ext} normalized by the physical cross-section $2D$ as a function of ρ' and wavelength for a cylinders pair with $D_o = 10$ nm. The color bar is in log-scale.

B. Nanofocusing properties

The electric field $\mathbf{E}'$ induced by the dimer can be deduced from the electrostatic potential solved in the original frame(Fig.8(b)). It can be decomposed as an infinite sum of modes $\mathbf{\Psi^{(n)}}$: $\mathbf{E}' = \sum_{n=1}^{\infty} \mathbf{\Psi^{(n)}}$. The analytical expression of the modes $\mathbf{\Psi^{(n)}}$ is derived in Ref.[74]. Note that in the near-field approximation, the enhancement of electric field is independent of the size of the system.

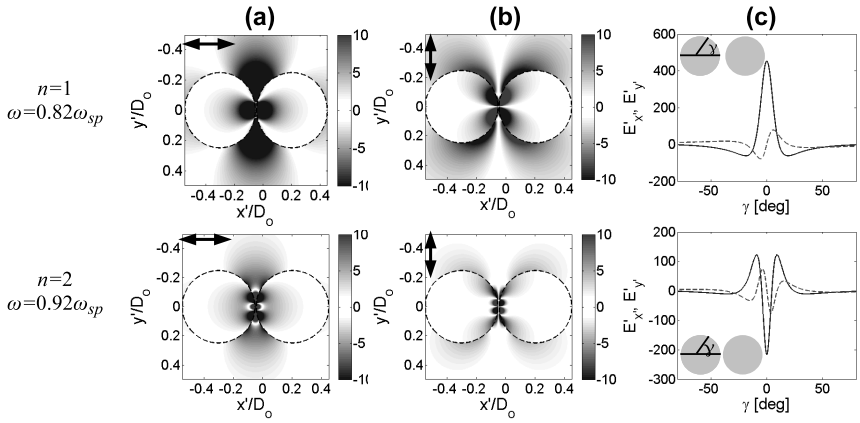

FIG. 15: Electric field for $\rho' = 10^{-2}$ associated with the two first modes $n = 1, 2$ (from top to bottom) at their corresponding resonant frequencies (Eq.25) for an incident wave polarized along x'. (a) Amplitude of the imaginary part of $\psi_{x'}^{(n)}$ normalized by the incoming field E_0' (polarized along x'). (b) Amplitude of the imaginary part of $\psi_{y'}^{(n)}$ normalized by the incoming field E_0' (polarized along y'). For (a) and (b) plots, the color scale is restricted to [-10 10] but note that the field magnitude can by far larger in the narrow gap between the structures. (c) Amplitude of the imaginary part of $\psi_{x'}^{(n)}/E_0'$ (blue) and $\psi_{y'}^{(n)}/E_0'$ (red) along the cylinder surface as a function of the angle γ defined in the figure.

Fig.15(a) and (b) represent the imaginary part of the field distribution along x' and y', respectively. These figures can be easily interpreted with CT. In the slab frame, the SP modes transport the energy of the dipoles along the surface of the metal slabs (see 8(b)). The same modes are excited in the transformed frame and propagate along the cylinder surface. As they approach the gap separating the two nanoparticles, the LSPs supported by each nanoparticle couple to each other, their wavelength shortens and group velocity decreases in proportion. This leads to an enhancement of the field in the narrow gap. However, contrary to the kissing cylinders (Sec.III), the velocity of LSPs does not vanish and energy cannot accumulate infinitely in the narrow gap. Instead, LSPs propagate indefinitely around the cylinders, leading to the resonant behavior pointed out previously.

Fig.15(c) represents the imaginary part of the field along the surface of the cylinders. The comparison between each mode allows to confirm our previous qualitative description: the angular momentum n associated to each mode corresponds to the number of spatial periods covered by the SP when propagating around one nanowire. Fig.15(c) also highlights the drastic field enhancement that can be induced within the gap between the two nanoparticles. Typically, for $\delta = D/50$, the field enhancement $|E'|/E_0$ can reach a value of 600. Note that the field enhancement is less than one order of magnitude of the value obtained for

kissing cylinders ($\sim 10^4$) (Fig.10(c)).

Note that the results displayed by Fig.14 and Fig.15 are valid in the quasi-static limit, *i.e* for $D < 20$ nm. In the next section, we show how to take into account the radiative losses in the CT picture and extend the range of validity of conformal mapping. Note also that the problem of a nanowire separated from a metal slab by an insulator thin layer (Fig.8(f)) has also been solved explicitly and the analytical details are presented in Ref.[74].

VI. BEYOND THE QUASI-STATIC APPROXIMATION

Until now, the CT approach has been quite restrictive since it can only apply to nanostructures of a few tens of nanometers (typically 20 nm). In this section, the range of validity of this approach is extended by taking into account the radiation damping [72]. The radiative losses are shown to map directly onto the power dissipated by a fictive absorbing particle in the original frame. We apply this approach to the case of the nanowire dimer studied in the previous section. Radiative losses are shown to limit the light harvesting process but improve its broadband feature. The field enhancement induced by the nanostructure decreases with the structure dimension but remains significant. In a second part, we take advantage of this strategy to study the interaction of a dipole emitter (*e.g* molecule or quantum dot) with complex plasmonic nanostructures by means of conformal mapping. The fluorescence enhancement as well as the quantum efficiency are derived analytically. Their spectral and spatial properties are analyzed in the perspective of experiments.

A. Conformal transformation picture

The aim of this section is show how to extend this CT approach to devices of much larger dimensions. Rigorously, this should be done by considering the magnetic component in addition to the electric field. However, this would be particularly tedious and intractable analytically since the permeability is not conserved under conformal mapping and should vary spatially as $1/r^2$ in the original frame [103]. We propose an alternative and finer route based on energy arguments [72]. It consists in extending the electrostatic results by taking into account the radiation damping. For simplicity but without loss of generality, we will consider the example of a dimer of nanowires illuminated by an incident plane wave $\mathbf{E_0'}$. A dipole $\mathbf{p}'$ is placed in the vicinity of the plasmonic system and accounts for the transition dipole moment of a fluorophore (Fig.16(a)). This complex problem can be mapped to a much simpler geometry through the transformation described in Fig.16 and already studied in the quasi-static limit in Sec.V.

In the dimer frame, the incoming beam is both absorbed and scattered by the nanostructure. The scattered field can be taken as uniform in the near field of the nanoparticles. Similarly to the incident field that is transformed into an array of dipoles in the slab frame, the counterpart of the scattered field in the slab geometry is an array of fictive absorbing particles, $\mathbf{\Delta}_s$, of polarizability $\gamma_s = -i\frac{\pi^2}{2}\epsilon_o g^2\omega^2/c^2$ [74], superimposed to the emitting dipoles $\mathbf{\Delta}$ (Fig.16(b)). These absorbers account for the radiative losses in the transformed geometry.

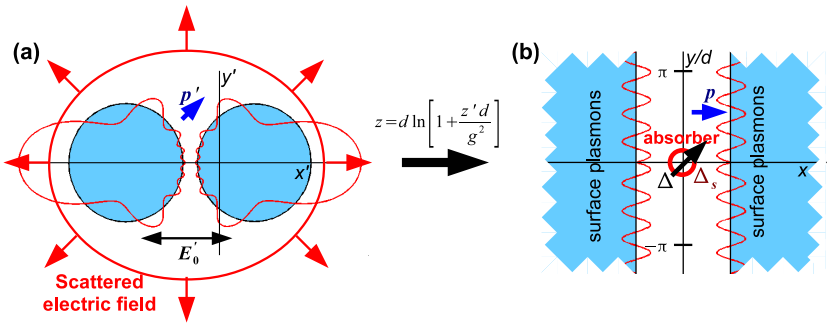

FIG. 16: (a) A pair of metallic nanowires of diameter D and separated by a distance δ is illuminated by an incident plane wave $\mathbf{E_0'}$. The dipole $\mathbf{p}'$ accounts for a fluorescent molecule placed in the vicinity of the nanostructure. (b) Using the transformation already described in Sec.II D, the latter system is transformed into two semi-infinite metallic slabs separated by a thin dielectric film. $\mathbf{E_0'}$ and $\mathbf{p}'$ are transformed into two dipoles $\mathbf{\Delta}$ and $\mathbf{p}$, respectively. An absorbing particle $\mathbf{\Delta_s}$ accounts for the radiative losses in the initial frame [72].

Radiative losses in the transformed geometry correspond to the power dissipated by this small absorber in the original frame. The radiative reaction is then considered to go beyond the electrostatic approximation. Taking into account the radiative reaction is necessary in order to satisfy the optical theorem (*i.e* energy conservation) [104]. In the transformed frame, it corresponds to the self-interaction between the particle and its own scattered field [104–106]. In the slab frame, the radiative reaction corresponds

to the field scattered by the fictive absorbing particle and back-emitted toward the metal slabs. The analytical results taking into account radiation damping will be presented in Sec.VI B and will be confronted to numerical simulations.

The fluorescent molecule $\mathbf{p}'$ located at z_0' in the dimer frame is transformed into an array of dipoles, whose location z_0 and dipole moment $\mathbf{p}$ are given by

$$z_0 = d \ln\left(1 + \frac{g^2}{z_0' d}\right), \quad \overline{p} = -\frac{g^2/z_0'^2}{1 + \frac{g^2}{z_0' d}} \overline{p'} \tag{39}$$

On the one hand, we will be able to study the total decay rate of the fluorescent molecule $\mathbf{p}'$ by investigating the total power of the dipole $\mathbf{p}$ dissipated in the slab frame. On the other hand, the radiative decay channel of $\mathbf{p}'$ will correspond to the power dissipated by each small absorber $\mathbf{\Delta_s}$ in the slab geometry. This problem will be treated in Sec.VI C.

B. Radiative losses

The introduction of a fictive absorbing particle at the origin of the slab frame allows to take into account radiation damping in the transformed frame. It yields the following expression for the extinction cross-section σ_{ext} of a dimer illuminated with a $x'-$polarized incident field [66]

$$\sigma_{ext} = \mathrm{Im}\left\{\frac{16\pi \frac{\omega}{c}\rho'(1+\rho')D^2\chi}{1 - i2\pi\rho'(1+\rho')D^2\frac{\omega^2}{c^2}\chi}\right\} \tag{40}$$

with the parameter χ defined in Eq.38. This expression should be compared with the previous expression of the absorption cross-section σ_a derived under the quasi-static limit (Eq.37). Radiation losses lead to a renormalization of σ_{ext} by the denominator of Eq.40. Fig.17(a) shows the effect of radiative damping on the extinction spectrum for different size of dimers at a fixed ratio $\rho' = \delta/(2D) = 0.01$. The theoretical predictions (Eq.40) are compared to the results of numerical simulations performed by D. Y. Lei with the software Comsol. An excellent agreement is found in the quasi-static limit ($D = 10$ nm). For larger structure dimensions, the numerical results are slightly red-shifted compared to our theoretical predictions. This is due to the retardation effects which are not considered by the CT approach [72]. However, the magnitude and line shape of resonances are nicely predicted for structure dimension up to 200 nm. Fig.17(a) shows that radiative damping broadens the line width of each resonance and leads to the saturation of the extinction cross-section at the level of the physical cross-section.

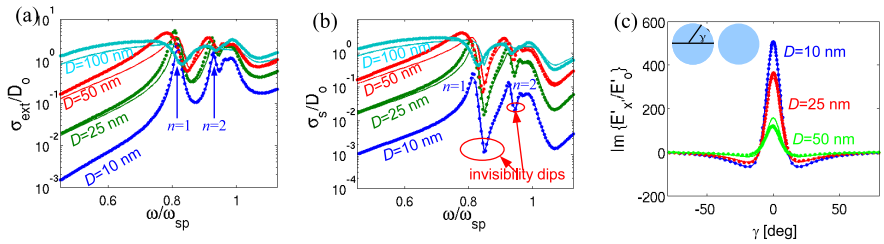

FIG. 17: Extinction cross-section σ_{ext} (a) and scattering cross-section σ_s (b), normalized by the physical cross-section $2D$, plotted as a function of frequency for nanowire dimers of different size with $\rho' = 0.01$. The theoretical predictions (continuous lines, Eqs.40-41) are compared to the results of numerical simulations (dots). (c)Imaginary part of $E'_{x'}/E'_0$ along the surface of the nanowire at the first resonant frequency $\omega = 0.8\omega_{sp}$, for $\rho' = 0.01$. The theoretical predictions (continuous lines, Eq.42) and numerical results (dots) are compared for different nanowire diameter D: 10 nm (blue), 25 nm (red), 50 nm (green). For all panels, the metal is assumed to be silver [92].

An expression of the scattering cross-section σ_s can also be derived by computing the power dissipated by the fictive absorber in the slab frame,

$$\sigma_s = \frac{32\pi^2 \frac{\omega^3}{c^3}\rho'^2(1+\rho')^2 D^4 |\chi|^2}{\left|1 - i2\pi\rho'(1+\rho')D^2\frac{\omega^2}{c^2}\chi\right|^2} \tag{41}$$

The radiative spectrum depends on $|\chi|^2$. Hence, the resonances defined by Eq.25 also occur in the scattering spectrum. This is confirmed by Fig.17(b) which displays $\sigma_s/(2D)$ as a function of frequency for different size of dimers at a fixed ratio $\rho' = 0.01$. There is a perfect agreement between our theoretical prediction and the numerical result in the quasi-static limit ($D = 10$ nm). The resonances displayed by Fig.17(b) clearly display an asymmetric line shape. We stress on the fact that these are not Fano

resonances which appear usually in the extinction spectrum and correspond to the coupling between bright and dark modes [107–110]. The sharp dips observed in Fig.17(b) originate from the destructive interference between each successive bright mode. Typically, the sharp dip observed at $\omega = 0.85\omega_{sp}$ results from the destructive interference between the modes $n = 1$ and $n = 2$ which resonate on each side of the dip [74]. This feature can be promising in perspective of sensing applications, since the ratio between the absorption and scattering cross-sections can reach for instance a value of 150 in the conditions considered in Fig.17(b). At these invisibility frequencies, the nanowire dimer can harvest light efficiently from the far-field and focus its energy at the nanoscale, without any scattering in the surrounding area. The dimer acts then as an invisible/non-invasive sensor. This idea is in relation with the concept of sensor cloaking proposed by Alú and Engheta [111]. Note that the dimer is invisible in all the directions except in the forward scattering one where the absorption of light will induce an attenuation of the incident beam.

As for the extinction cross-section, radiation damping leads to a renormalization of the scattering cross-section for large structure dimensions (see the denominator in Eq.41) which makes σ_s saturate at the level of the physical cross-section (see Fig.17(b)). A satisfying agreement is found between numerical and analytical results in Fig.17(b), except for the slight red shift explained by retardation effects. The Q-factor of the invisibility dips decreases for large structure dimensions and the nanowire dimer may keep its invisible feature only for nanowire diameter inferior to 50 nm.

In the quasi-static limit, the near-field enhancement does not depend on the size of the device. However, radiative damping breaks this property and limits the nanofocusing properties of the dimer. Radiative reaction requires the renormalization of the electric field by a factor ζ [74]

$$\zeta = 1 - 2i\pi\rho'(1+\rho')D^2\frac{\omega^2}{c^2}\chi \tag{42}$$

The effect of the radiative losses on the field enhancement is shown in Fig.17(c). The imaginary part of $E'_{x'}/E'_0$ along the surface of the nanowire is displayed at the first resonant frequency $\omega = 0.8\omega_{sp}$, for $\rho' = 0.01$. The theoretical and numerical results are compared for different dimensions $D = 10$, 25, 50 nm and a good agreement is found. The radiation losses lead to a renormalization of the electric field by the factor ζ which increases with the structure dimension (Eq.42). For $D = 50$ nm, a slight disagreement starts to appear between theory and numerical simulations, due to the retardation effects which are not taken into account by our model [72].

Note that the same strategy can be applied to determine the radiative losses in all the structures that can be derived *via* conformal mapping. For instance, the effect of radiative damping has been studied analytically for kissing nanowires as well [72].

C. Fluorescence enhancement

We now apply the CT strategy beyond the quasi-static limit to predict analytically the fluorescence enhancement for molecules placed in the vicinity of metallic nanostructures. We first briefly recall the main point of the spontaneous emission by a molecule in the near-field of a nanoantenna. Then we will show how the CT approach can be used to predict analytically the fluorescence enhancement of molecules placed in the vicinity of metallic nanostructures. As the absorption and emission process occur at different frequencies, a perfect knowledge of the spectral and spatial properties of the field enhancement might be decisive for the implementation of new types of biosensors.

1. Fluorescence enhancement in the near-field of nano-antenna

A plasmonic device can strongly influence the fluorescence of a molecule placed in its near-field [44, 112–116]. On the one hand, LSPs can induce intense fields at the nano-scale that are likely to increase the number of photons absorbed by a molecule at its excitation frequency. On the other hand, at the emission frequency, the radiative and non-radiative properties of the emitter strongly depend on its environment. This is the so-called Purcell effect [117]. The interplay between local-field enhancements, radiative and nonradiative decay channels can lead to an enhancement of the fluorescence signal or to quenching.

The fluorescence emission by a molecule is governed by an important parameter, the decay rate γ, which describes the amplitude decay suffered by the transition dipole of the molecule in time. Two contributions to this overall decay can be identified: γ^R is the radiative decay rate that gives rise to the emission of a photon in the far field, γ_{int}^{NR} is an intrinsic nonradiative decay rate that accounts for internal losses. The emission efficiency of a fluorophore is then quantified by the intrinsic quantum yield:

$$\eta_0 = \frac{\gamma_R^o}{\gamma^o} = \frac{\gamma_R^o}{\gamma_R^o + \gamma_{NR}^o} \tag{43}$$

The quantum yield represents the probability that an excited fluorescent molecule emits one photon. The presence of a nanoparticle in the vicinity of the emitter can modify the quantum yield of the molecule, such that

$$\eta = \frac{\gamma_R}{\gamma} = \frac{\gamma_R}{\gamma_R + \gamma_{NR} + \gamma^o_{NR}} \tag{44}$$

We can identify three different decay channels in the system now: the radiative rate, γ_R, the external nonradiative decay rate induced by dissipation in the metal, γ_{NR}, and the nonradiative decay rate intrinsic to the emitter, γ^o_{NR}. A metallic nanostructure sustains highly confined modes and induces strong radiative losses. Hence, it may give rise to a large enhancement of the radiative decay rate experienced by any emitter placed in its vicinity. The ratio γ_R/γ^o_R is usually termed as the Purcell factor.

The fluorescence of a molecule is given by the product of two different factors: the emitter quantum yield, η, which measures its ability to re-radiate once excited, and the EM energy that it is able to absorb from the incident electric field in the excitation process, which is proportional to $|\mathbf{p}'.\mathbf{E}'|^2$ (where $\mathbf{p}'$ is the transition dipole moment, and $\mathbf{E}'$ is the electric field evaluated at the emitter position). The fluorescence enhancement then reads

$$S/S_0 = \left(\eta \left|\mathbf{p}'.\mathbf{E}'\right|^2\right) / \left(\eta_0 \left|\mathbf{p}'.\mathbf{E}'_{\mathbf{0}}\right|^2\right) \tag{45}$$

The radiative decay rate γ_R is proportional to the power radiated in the far field, while the nonradiative decay rate γ_{NR} is proportional to the power absorbed by the metallic nanostructures.

2. The CT approach

As an example, we consider the interaction of a fluorophore with a dimer of nanowires as already described in Fig.16. To solve this problem, this configuration is mapped onto a much simpler one consisting of a dipole sandwiched between two semi-infinite metal slabs (Fig.16(b)). The solution in the latter geometry allows to derive analytically different quantities such that the fluorescence enhancement as well as the quantum efficiency in presence of the metallic nanostructure. Note that previous works have investigated theoretically similar problems [44, 118, 119] but none of them have led to a full analytical solution.

The radiative decay rate is proportional to the power radiated by the nanostructure. In the slab frame(Fig.16(a)), it consists in calculating the power dissipated by the small absorber accounting for radiative losses. Normalizing it by the power radiated by the molecule in free space leads to the Purcell factor γ_R/γ^o_R. The wave-length dependence of the Purcell factor is displayed in Fig.18(a) for a transition dipole moment $\mathbf{p}'$ aligned along x' and located at the center of the gap. The Purcell factor displays dramatic peaks ($> 10^7$) at the LSPs resonances (Eq.25). Fig.18(b) and (c) show the spatial dependence of the Purcell factor for a transition dipole moment $\mathbf{p}'$ aligned along x' and y', respectively. These graphs are shown at the first LSP resonance($n = 1$) for a gap $\delta = D/50$ between the two nanowires. The Purcell factor displays strong spatial variations in the near-field of the nanowire with the highest values within the gap. These results show the extreme tunability of the Purcell factor according to the dipole position and the wave-length.

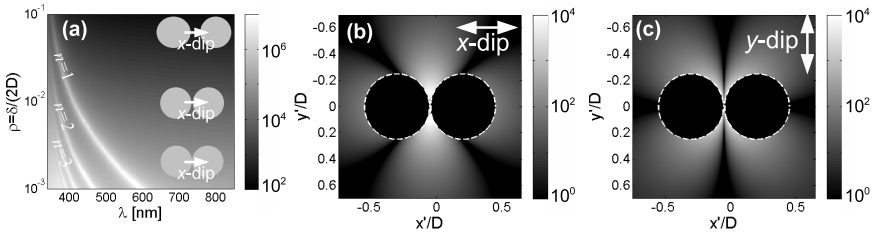

FIG. 18: Purcell factor for a dimer of silver nanowires (with $D = 20$ nm, permittivity taken from Ref.[92]). (a) Wavelength-dependence of the Purcell factor as a function of the distance between the two nanowires for a fluorophore placed exactly at the the center of the gap and a transition dipole moment aligned along x'. (b) and (c) Spatial dependence of the Purcell factor at the first resonance frequency ($n = 1$) for a transition dipole moment aligned along x' and y', respectively. The dimer size is 20 nm and the gap δ is $D/50$.

The quantum yield is an important parameter for future experiments. It can be computed through the CT approach by calculating the ratio between the power dissipated by the small absorber accounting for radiative damping (proportional to the radiative decay rate) and the total power dissipated by the array of dipoles $\mathbf{p}$ in the slab frame (proportional to the total decay rate). This is valid under the assumption that the nonradiative decay rate intrinsic to the emitter, γ^o_{NR}, is negligible compared to the nonradiative decay rate due to the dissipation losses in the metal, γ^o_{NR}. Fig.19(a) and (b) show the spatial dependence of the quantum yield η (Eq.44) for a transition dipole moment $\mathbf{p}'$ aligned along x' and y', respectively. These graphs are shown at the

first LSP resonance($n = 1$) for a gap $\delta = D/50$ between the two nanowires. Similarly to the Purcell factor, the quantum yield displays strong variations in the near-field of the dimer. For a transition dipole moment oriented along x', the quantum yield is maximum at the exact center of the gap but strongly decrease when the molecule move along the axis of symmetry of the dimer. The lines defined by $y' = \pm x'$ correspond to the area outside of the gap where a molecule, whose dipole moment is oriented along the x'-axis, is quenched. For a dipole moment oriented along the $y'-$axis, the molecule is quenched if it is placed along the axis of the dimer, hence in the gap as well.

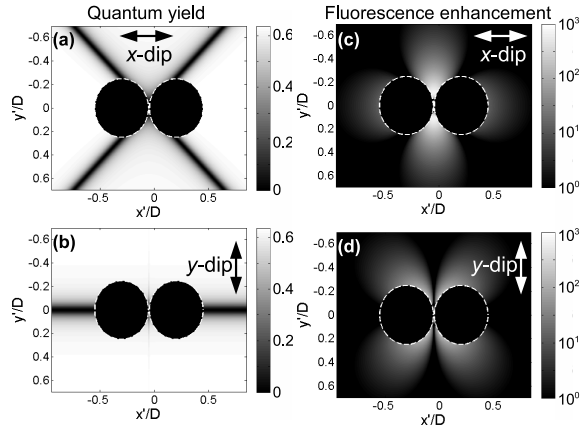

FIG. 19: Fluorescent properties of a molecule placed in the vicinity of a dimer of silver nanowires at the first resonance $n = 1$ (with $D = 20nm$, $\delta = D/50$, permittivity taken from Ref.[92]). (a),(c) Spatial variations of the quantum yield for a dipole oriented along x' and y', respectively. (b),(d) Spatial variations of the fluorescence enhancement for a dipole oriented along x' and y', respectively. The intrinsic quantum yield η_0 has been fixed to 0.66.

Fig.19(c) and (d) show the fluorescence enhancement (Eq.45) in the same conditions as for the quantum yield (Fig.19(a) and (b)), assuming that the absorption and emission process occur at the first resonance frequency of the dimer. Of course, this is a strong hypothesis but, note that, in practice, different absorption and emission frequencies can be incorporated in the model according to the fluorophore used in the experiment. The intrinsic quantum yield η_0 has been arbitrarily fixed to 0.66. Again, the fluorescence enhancement highly depends on the position of the fluorophore and on the orientation of its dipole moment. Maximal values for the fluorescence enhancement (up to 10^5) occur in the gap for a dipole oriented along x'. Hence, plasmon hybridization offers spectral and spatial degrees of freedom that can be used to tune the fluorescence and the apparent quantum yield with high sensitivity.

To conclude, note that the CT strategy is really powerful since it provides a fully analytical solution to describe the physics of the interaction between a fluorophore and a plasmonic nanostructure. Unlike a numerical approach, an efficient and rapid optimization of the nanostructures can be performed. Our analytical model predicts quantitatively the quantum yield and the fluorescence enhancement induced by these metallic structures for nanowire diameters below 100 nm. As the absorption and emission process occur at different frequencies, a perfect knowledge of the spectral and spatial properties of the field enhancement might be decisive for the implementation of an experimental setup aiming at single molecule detection. The main perspective of this work is to extend this study to a 3D configuration and in particular to consider a 3D dipole rather than a 2D dipole, which has not physical existence. We believe our 2D model provides a qualitative knowledge for the spatial and wavelength dependence of the Purcell factor, the quantum yield and the fluorescence enhancement. However, note that the values provided here are not quantitative predictions of what would happen for a 3D transition dipole moment like in a real experiment.

VII. NON-LOCAL EFFECTS

Conformal mapping designs a path towards the plasmonics *graal*, *i.e* a broadband light harvesting accompanied with a drastic focusing of light at the nanoscale (see Sec.III-IV). However, the nanostructures derived by conformal mapping display geometrical singularities in which the spatial extent of the EM fields is comparable to the Coulomb screening length in noble metals (δ_c =0.1 nm for silver [120]). From a theoretical perspective, the study of SPs in the vicinity of such singularities requires the implementation of non-local, spatially dispersive permittivities that take into account the effect of electron-electron interactions in the dielectric response of the metal. In a recent study, A. Fernández-Domínguez *et al.* have adapted the CT approach to investigate the impact of non-locality on the optical properties of singular plasmonic nanostructures [69]. This section is dedicated to the review of this theoretical breakthrough.

A. Conformal mapping of non-locality

A. Fernández-Domínguez *et al.* have shown in particular how the spatially dispersive character of the metal permittivity can be considered in the CT leading to kissing nanowires (see Sec.II B) [69]. Fig.20(b) depicts the system under study, a pair of touching

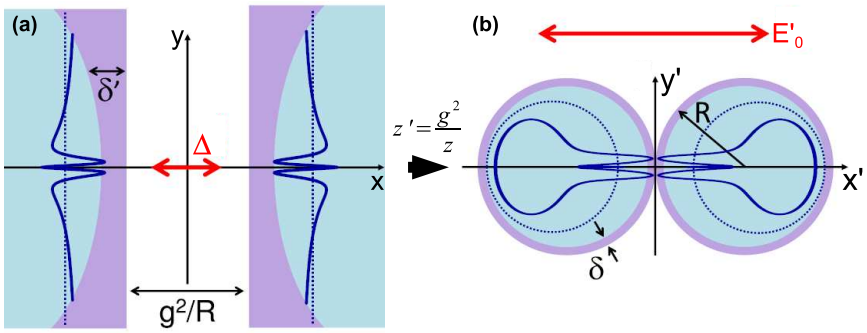

FIG. 20: Figure courtesy of A. Fernández-Domínguez [69]. Conformal map transforming a MIM structure (a) into kissing nanowires (b) with a non-local description of the interaction of light with the nanostructure. The shaded areas in both panels represent the decay length of the longitudinal plasmons excited in the system. Blue solid lines show artistic plots of the electrostatic potential describing propagating SPPs in both frames.

nanowires illuminated by a plane wave polarized along the dimer axis, as already investigated under the local approximation in Sec.III. Now, the metal permittivity is modeled using the so-called hydrodynamical Drude model [121], which yields the following dielectric functions ϵ'_T and ϵ'_M for transverse and longitudinal EM fields, respectively

$$\epsilon'_T(\omega) = \epsilon_\infty \left[1 - \frac{\omega_P^2}{\omega(\omega + i\gamma)}\right], \quad \epsilon'_L(\omega, \mathbf{k}) = \epsilon_\infty \left[1 - \frac{\omega_P^2}{\omega(\omega + i\gamma) - \xi'^2 |\mathbf{k}|^2}\right] \tag{46}$$

The usual Drude constants are obtained from the fitting to experimental data for silver [102], whereas ξ', which measures the degree of non-locality, is set as a free parameter for the moment. The dark ring in Fig.20(b) accounts for the decay length of the longitudinal plasmons into the metal, $\delta' \sim \frac{\xi'}{\omega_p}$ ($\omega << \omega_p$). δ' represents the extension of the surface charges induced in the nanowires by the incident light.

Through the conformal inversion (Eq.5), the problem consisting in an incident field illuminating the touching nanowires (Fig.20(b)) map onto a dipole sandwiched between two semi-infinite metallic slabs (Fig.20(a)). Whereas $\epsilon'_T(\omega)$ is preserved under the transformation, the $\mathbf{k}'-$dependence of $\epsilon'_L(\omega, \mathbf{k}')$ makes it sensitive to the inversion. Assuming that the non-local length scale is much smaller than the spatial range in which dz/dz' varies significantly, the general relation between the original longitudinal permittivity and its transformed counterpart reads [69]

$$\epsilon_l(\mathbf{k}, \omega) = \epsilon'_l\left(\left|\frac{dz}{dz'}\right| \mathbf{k}, \omega\right) \tag{47}$$

Hence, conformal mapping leads to a wave-vector stretching weighted by $|dz/dz'|$ and to a longitudinal permittivity characterized by a degree of non-locality $\xi(z) = \xi'|z|^2/g^2$. The surface charge thickness δ in the slab frame now exhibits a $y'-$dependence (Fig.20(b)). The problem in the slab frame is solved under the so-called eikonal (WKB) approximation [69]. This assumption relies on the fact that $\delta(y)$ varies in space much more slowly than the oscillating EM fields. Note that this approach omits electron tunnelling effects, which could have some influence in the plasmonic response of nanoparticle dimers as well [101].

B. Towards the physics of local dimers

Solving the problem in the slab frame leads to an analytical solution for the non-local kissing nanowires problem. The analytical expressions of the absorption cross-section and the field enhancement can be found in the original article [69]. Here we will present the main results and insist on the physics hidden behind them. The plasmonic behavior of non-local touching nanowires is qualitatively different from the local prediction. In the local approximation there is a continuous spectrum of modes that propagate towards the touching point but can never reach it. In the non-local description, the modes can sneak past the touching point and circulate round and round the structure. Hence the spectrum is now discrete and the physics is closely related to the case of non-touching local nanowires (see Sec.V).

Fig.21(a) displays the absorption spectra for a $R = 10$ nm nanowire dimer. Analytical results are compared to numerical ones obtained with COMSOL. For comparison, σ_a is also displayed for a local dimer (grey), local (solid black) and non-local ($\delta = 10^{-2}\lambda_p$, dashed line) single nanowires. Whereas non-locality only blueshifts the dipolar resonance of isolated nanowires, it gives rise to a set of absorption peaks for kissing nanowires. These non-local resonances shift to higher frequencies when ξ increases, in a similar manner as the dipolar peak of a single nanowire. Importantly, Fig.21(a) shows that the broadband response of touching dimers is lost at frequencies below the lowest non-local resonance. Fig.21(b) plots the field enhancement along the nanowire surface evaluated at the three first resonances for a value of $\delta' = 10^{-3}\lambda_p$ (green line in Fig.21(a)). In analogy with non-touching local nanowires (Sec.V), the rank n of the modes can be related to the number of nodes that the SPP fields present near the singularity. Note that the non-local effects drastically reduce the maximum field enhancement that can be reached (typically 2×10^2 instead of 2×10^4 under the local approximation). The electric field now spreads over a larger range of angles than under the local approximation. The good point is that the area of field amplification will be much more accessible to molecules in surface enhanced Raman-scattering and fluorescence enhancement experiments.

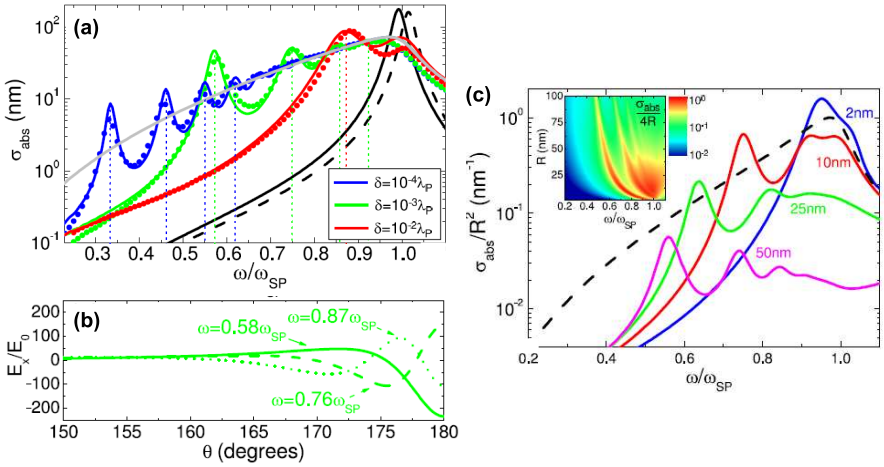

FIG. 21: Figures courtesy of A. Fernández-Domínguez [69]. (a): Theoretical (solid lines) and numerical (dots) absorption spectra for 10 nm radii non-local nanowires compared with the cross section obtained within the local approximation (grey dashed line). σ_a for a local (non-local, $\delta = 10^{-2}\lambda_p$) single nanowire is also plotted in solid (dashed) black line. (b) Field enhancement close to the touching point at the three lowest non-local resonances for $\delta = 10^{-3}\lambda_p$ (value appropriate for silver). (c) Absorption cross section normalized to the structure area for Ag ($\beta = 3.6 \times 10^{-3}c$) for nanowires of different radii. Color solid lines plot the non-local results and dashed black line corresponds to the electrostatic local result for all R. The inset shows the absorption efficiency versus the incident frequency and nanowires radius.

Fig.21(c) shows the absorption spectra normalized to R^2 for various nanowire sizes (color solid lines). Within the electrostatic local approximation (Eq.28) [45], σ_a scales as R^2, hence plotting σ_a/R^2 allows to investigate simultaneously non-local and radiative effects on the optical properties of the system. Radiation damping is taken into account incorporating a fictive absorber in the slab frame (see Sec.VI). The comparison between the non-local results and the electrostatic local prediction clarifies how non-locality and radiation losses modify the optical properties of the system. For small sizes ($R = 2$ nm), radiation is negligible, but the weight of spatial dispersion, δ'/R, is high. The absorption spectrum shows a single peak with a narrow line width like a single nanowire (see Fig.21(a)). For larger sizes, the absorption cross-section decreases compared to the electrostatic prediction due to radiative reaction, while the impact of non-locality is diminished. Thus, the dimers interact less efficiently with the incoming light, but over a larger bandwidth. In the inset, the absorption efficiency σ_a/R is shown as a function of ω/ω_{sp} and the nanowire radius R. The light collection performance of the structure is optimized for nanowire radii between 5 and 50 nm, where the balance between radiative and non-local effects is the most convenient.

Note that the study of non-locality with conformal mapping is not restricted to the case of kissing nanowires but can be extended to all the singular structures mentioned earlier in the review and displayed in Figs.2 and 5.

VIII. SUMMARY AND OUTLOOK

To briefly conclude, this review shows how CT provides an elegant tool to design plasmonic structures capable of an efficient harvesting of light over the whole visible spectrum. SP modes are shown to propagate toward the structure singularity where their velocity vanishes and energy accumulates. Strong field enhancement ($> 10^3$) and confinement at the nano-scale have been predicted within the classical approach. Subsequent refinements of the CT theory has allowed to take into account the bluntness of the nanostructure that will be inevitable in practice, as well as radiative losses and non-locality. The consideration

of these limits makes the CT approach really powerful, capable of predicting analytically the optical properties of a large variety of nanostructures and designing a path towards a broadband nanofocusing of light. Experiments are currently performed to confirm the theoretical predictions [42, 122, 123]. The proposed plasmonic nanostructures may find great potential applications in solar cells [124–126], surface-enhanced Raman scattering [91, 127], single molecule detection [128, 129], plasmon-controlled fluorescence [44, 112–116], high-harmonic generation [26], and SPASERS [85, 130].

IX. ACKNOWLEDGMENTS

The authors wish to thank Dang Yuan Lei, Yu Luo, Antonio Fernández-Domínguez, Yannick Sonnefraud and Stefan Maier for all the collaborative work and the fruitful discussions within the framework of the *transformation optics for plasmonics* project at Imperial College. This work was supported by the European Community project PHOME (Contract No. 213390) and by the U.K. Engineering and Physical Sciences Research Council (EPSRC).

[1] G. Mie. Beiträge zur optik trüber medien, speziell kolloidaler metallösungen. *Ann. Phys.*, 25:377–445, 1908.
[2] R. H. Ritchie. Plasma losses by fast electrons in thin films. *Phys. Rev.*, 106:874–881, 1957.
[3] H. Raether. *Surface Plasmons on Smooth and Rough Surfaces and on Gratings*. Springer, Berlin, 1988.
[4] U. Kreibig and M. Vollmer. *Optical Properties of Metal Clusters*. Springer, Berlin, 1995.
[5] S.A. Maier. *Plasmonics: Fundamentals and Applications*. Springer, New York, 2007.
[6] S. A. Maier and H. A. Atwater. Plasmonics: Localization and guiding of electromagnetic energy in metal/dielectric structures. *J. Appl. Phys.*, 98:011101, 2005.
[7] J. B. Pendry. Negative refraction makes a perfect lens. *Phys. Rev. Lett.*, 85:3966–3969, 2000.
[8] N. Fang, H. Lee, C. Sun, and X. Zhang. Subdiffraction-limited optical imaging with a silver superlens. *Science*, 308:534–537, 2005.
[9] K. L. Kelly, E. Coronado, L. L. Zhao, and G. C. Schatz. The optical properties of metal nanoparticles: The influence of size, shape, and dielectric environment. *J. Phys. Chem. B*, 107:668–677, 2003.
[10] E. Hao and G.C. Schatz. Electromagnetic fields around silver nanoparticles and dimers. *J. Chem. Phys.*, 120:357–366, 2003.
[11] J.P. Kottmann and O.J.F. Martin. Plasmon resonant coupling in metallic nanowires. *Opt. Exp.*, 8:655–663, 2001.
[12] K.-H. Su, Q.-H. Wei, X. Zhang, J. J. Mock, D. R. Smith, and S. Schultz. Interparticle coupling effects on plasmon resonances of nanogold particles. *Nano Lett.*, 3:1087–1090, 2003.
[13] K. Li, M. I. Stockman, and D. J. Bergman. Self-similar chain of metal nanospheres as an efficient nanolens. *Phys. Rev. Lett.*, 91:227402, 2003.
[14] T. Atay, J.-H. Song, and A. V. Nurmikko. Strongly interacting plasmon nanoparticle pairs: From dipole-dipole interaction to conductively coupled regime. *Nano Lett.*, 4:1627–1631, 2004.
[15] P. Nordlander, C. Oubre, E. Prodan, K. Li, and M.I. Stockman. Plasmon hybridization in nanoparticle dimers. *Nano Lett.*, 4:899–903, 2004.
[16] C. E. Talley, J. B. Jackson, C. Oubre, N. K. Grady, C. W. Hollars, S. M. Lane, T. R. Huser, and P. Nordlander. Surface-enhanced Raman scattering from individual Au nanoparticles and nanoparticle dimer substrates. *Nano Lett.*, 5:1569–1574, 2005.
[17] L.A. Sweatlock, S.A. Maier, H.A. Atwater, J.J. Penninkhof, and A. Polman. Highly confined electromagnetic fields in arrays of strongly coupled Ag nanoparticles. *Phys. Rev. B*, 71:235408, 2005.
[18] I. Romero, J. Aizpurua, G.W. Bryant, and F.J. García de Abajo. Plasmons in nearly touching metallic nanoparticles. *Opt. Exp.*, 14:9988–9999, 2006.
[19] I. Romero, T.V. Teperik, and F.J. García de Abajo. Plasmon molecules in overlapping nanovoids. *Phys. Rev. B*, 77:125403, 2008.
[20] J. Britt Lassiter, J. Aizpurua, L.I. Hernandez, D.W. Brandl, I. Romero, S. Lal, J.H. Hafner, P. Nordlander, and N.J. Halas. Close encounters between two nanoshells. *Nano Lett.*, 8:1212–1218, 2008.
[21] T. Härtling, Y. Alaverdyan, A. Hille, M. T. Wenzel, M. Käll, and L. M. Eng. Optically controlled interparticle distance tuning and welding of single gold nanoparticle pairs by photochemical metal deposition. *Opt. Express*, 16:12362, 2008.
[22] L. Yang, B. Yan, and B. M. Reinhard. Correlated optical spectroscopy and transmission electron microscopy of individual hollow nanoparticles and their dimers. *J. Phys. Chem. C*, 112:15989–15996, 2008.
[23] M. P. Busson, B. Rolly, B. Stout, N. Bonod, E. Larquet, A. Polman, and S. Bidault. Optical and topological characterization of gold nanoparticle dimers linked by a single DNA double strand. *Nano Lett.*, 11:5060–6065, 2011.
[24] N. J. Halas, S. Lal, W.-S. Chang, S. Link, and P. Nordlander. Plasmons in strongly coupled metallic nanostructures. *Chem. Rev.*, 111:3913–3961, 2011.
[25] Y. Lu, G.L. Liu, J. Kim, Y.X. Mejia, and L.P. Lee. Nanophotonic crescent moon structures with sharp edge for ultrasensitive biomolecular detection by local electromagnetic field enhancement effect. *Nano Lett.*, 5:119–124, 2005.
[26] J. Kim, G.L. Liu, Y. Lu, and L.P. Lee. Intra-particle plasmonic coupling of tip and cavity resonance modes in metallic apertured nanocavities. *Opt. Exp.*, 13:8332–8338, 2005.
[27] H. Rochholz, N. Bocchio, and M. Kreiter. Tuning resonances on crescent-shaped noble-metal nanoparticles. *New J. Phys.*, 9:53, 2007.
[28] R. Bukasov and J.S. Shumaker-Parry. Highly tunable infrared extinction properties of gold nanocrescents. *Nano Lett.*, 7:1113–1118, 2007.

[29] B. M. Ross and L. P. Lee. Plasmon tuning and local field enhancement maximization of the nanocrescent. *Nanotechnology*, 19:275201, 2008.

[30] L. Feng, D. Van Orden, M. Abashin, Q-J. Wang, Y-F. Chen, V. Lomakin, and Y. Fainman. Nanoscale optical field localization by resonantly focused plasmons. *Opt. Exp.*, 17:4824–4832, 2009.

[31] L. Y. Wu, B.M. Ross, and L.P. Lee. Optical properties of the crescent-shaped nanohole antenna. *Nano Lett.*, 9:1956–1961, 2009.

[32] R. Bukasov, T. A. Ali, P. Nordlander, and J. S. Shumaker-Perry. Probing the plasmonic near-field of gold nanocrescent antennas. *ACS Nano*, 4:6639–6650, 2010.

[33] S.J. Oldenburg, R.D. Averitt, S.L. Westcott, and N.J. Halas. Nanoengineering of optical resonances. *Chem. Phys. Lett.*, 288:243–247, 1998.

[34] R. D. Averitt, S. L. Westcott, and N. J. Halas. Linear optical properties of gold nanoshells. *J. Opt. Soc. Am. B*, 16:1824–1832, 1999.

[35] C. Graf and A. van Blaaderen. Metallodielectric colloidal core-shell particles for photonic applications. *Langmuir*, 18:524–534, 2001.

[36] E. Prodan, C. Radloff, N. J. Halas, and P. Nordlander. A hybridization model for the plasmon response of complex nanostructures. *Science*, 302:419–422, 2003.

[37] Y. Sun, B. Wiley, Z.-Y. Li, and Y. Xia. Synthesis and optical properties of nanorattles and multiple-walled nanoshells/nanotubes made of metal alloys. *J. Am. Chem. Soc.*, 126:9399–9406, 2004.

[38] L. R. Hirsch, A. M. Gobin, A. R. Lowery, F. Tam, R. A. Drezek, N. J. Halas, and J. L. West. Metal nanoshells. *Ann. Biomed. Eng.*, 34:15–22, 2006.

[39] F.J. García-Vidal and J.B. Pendry. Collective theory of surface enhanced Raman scattering. *Phys. Rev. Lett.*, 77:1163–1166, 1996.

[40] K. Li, L. Clime, B. Cui, and T. Veres. Surface enhanced Raman scattering on long-range ordered noble-metal nanocrescent arrays. *Nanotechnology*, 19:145305, 2008.

[41] G. L. Liu, Y. Lu, J. Kim, and L. P. Lee J. C. Doll. Magnetic nanocrescents as controllable surface-enhanced Raman scattering nanoprobes for biomolecular imaging. *Adv. Mater.*, 17:2683–2688, 2005.

[42] R. T. Hill, J. J. Mock, Y. Urzhumov, D. S. Sebba, S. J. Oldenburg, S.-Y. Chen, A. A. Lazarides, A. Chilkoti, and D. R. Smith. Highly confined electromagnetic fields in arrays of strongly coupled Ag nanoparticles. *Nano Lett.*, 10:4150–4154, 2010.

[43] J. Zhang, Y. Fu, M. H. Chowdhury, and J. R. Lakowicz. Metal-enhanced single-molecule fluorescence on silver particle monomer and dimer: Coupling effect between metal particles. *Nano Lett.*, 7:2101–2107, 2007.

[44] C. Vandenbem, D. Brayer, L. S. Frouze-Pérez, and R. Carminati. Controlling the quantum yield of a dipole emitter with coupled plasmonic modes. *Phys. Rev. B*, 81:085444, 2010.

[45] A. Aubry, D. Y. Lei, A. Fernandez-Dominguez, Y. Sonnefraud, S. A. Maier, and J. B. Pendry. Plasmonic light-harvesting devices over the whole visible spectrum. *Nano Lett.*, 10:2574–2579, 2010.

[46] A. J. Ward and J. B. Pendry. Refraction and geometry in maxwell's equations. *J. Mod. Opt.*, 43:773–793, 1996.

[47] D.M. Shyroki. Note on transformation to general curvilinear coordinates for maxwell's curl equations. *arXiv:physics/0307029v1*, 2007.

[48] N. B. Kundtz, D. R. Smith, and J. B. Pendry. Electromagnetic design with transformation optics. *Proceedings of the IEEE*, 99:1622–1633, 2011.

[49] U. Leonhardt. Optical conformal mapping. *Science*, 312:1777–1780, 2006.

[50] J. B. Pendry, D. Schurig, and D. R. Smith. Controlling electromagnetic fields. *Science*, 312:1780–1782, 2006.

[51] D. Schurig, J. J. Mock, B. J. Justice, S. A. Cummer, J. B. Pendry, A. F. Starr, and D. R. Smith. Metamaterial electromagnetic cloak at microwave frequencies. *Science*, 314:977–980, 2006.

[52] J. Li and J. B. Pendry. Hiding under the carpet: A new strategy for cloaking. *Phys. Rev. Lett.*, 101:203901, 2008.

[53] R. Liu, C. Ji, J. J. Mock, J. Y. Chin, T. J. Cui, and D. R. Smith. Broadband ground-plane cloak. *Science*, 323:366–369, 2009.

[54] J. Valentine, J. Li, T. Zentgraf, G. Bartal, and X. Zhang. An optical cloak made of dielectrics. *Nature Mater.*, 8:568–571, 2009.

[55] L. H. Gabrielli, J. Cardenas, C. B. Pointras, , and M. Lipson. Silicon nanostructure cloak operating at optical frequencies. *Nat. Photonics*, 3:461–463, 2009.

[56] T. Ergin, N. Stenger, P. Brenner, J. B. Pendry, and M. Wegener. Three-dimensional invisibility cloak at optical wavelengths. *Science*, 328:337–339, 2010.

[57] P. A. Huidobro, M. L. Nesterov, L. Martín-Moreno, and F. J. García-Vidal. Transformation optics for plasmonics. *Nano Lett.*, 10:1985–1990, 2010.

[58] Y. Liu, T. Zentgraf, G. Bartal, and X. Zhang. Transformational plasmon optics. *Nano Lett.*, 10:1991–1997, 2010.

[59] J. Renger, M. Kadic, G. Dupont, S. S. Aćimović, S. Guenneau, R. Quidant, and S. Enoch. Hidden progress: Broadband plasmonic invisibility. *Opt. Express*, 18:15757–15768, 2010.

[60] T. Zentgraf, Y. Liu, M. H. Mikkelsen, J. Valentine, and X. Zhang. Plasmonic Luneburg and Eaton lenses. *Nature Nanotech.*, 6:151–155, 2011.

[61] P. A. Huidobro, M. L. Nesterov, L. Martín-Moreno, and F. J. García-Vidal1. Moulding the flow of surface plasmons using conformal and quasiconformal mappings. *New J. Phys.*, 13:033011, 2011.

[62] J. Zhang, S. Xiao, M. Wubs, and N. A. Mortensen. Surface plasmon wave adapter designed with transformation optics. *ACS Nano*, 5:4359–4364, 2011.

[63] M. Kadica, G. Dupont, S. Guenneau, and S. Enoch. Controlling surface plasmon polaritons in transformed coordinates. *J. Mod. Opt.*, 58:994–1003, 2011.

[64] M. Gharghi, C. Gladden, T. Zentgraf, Yongmin Liu, X. Yin, J. Valentine, and Xiang Zhang. A carpet cloak for visible light. *Nano Lett.*, 11:2825–2828, 2011.

[65] Y. Luo, J. B. Pendry, and A. Aubry. Surface plasmons and singularities. *Nano Lett.*, 10:4186–4191, 2010.

[66] A. Aubry, D. Y. Lei, S. A. Maier, and J. B. Pendry. Interaction between plasmonic nanoparticles revisited with transformation optics. *Phys. Rev. Lett.*, 105:233901, 2010.

[67] A. Fernández-Domínguez, S. A. Maier, and J. B. Pendry. Collection and concentration of light by touching spheres: A transformation

optics approach. *Phys. Rev. Lett.*, 105:266807, 2010.
[68] Y. Luo, D. Y. Lei, S. A. Maier, and J. B. Pendry. Broadband light harvesting nanostructures robust to edge bluntness. *Phys. Rev . Lett.*, 108:023901, 2012.
[69] A. Fernández-Domínguez, S. A. Maier, and J. B. Pendry. Transformation optics description of non-local effects in plasmonic nanostructures. *submitted to Phys. Rev. Lett.*, 2012.
[70] D. Y. Lei, A. Aubry, S. A. Maier, and J. B. Pendry. Broadband nano-focusing of light using kissing nanowires. *New J. Phys.*, 12:093030, 2010.
[71] A. Aubry, D. Y. Lei, S. A. Maier, and J. B. Pendry. Broadband plasmonic device concentrating the energy at the nanoscale: The crescent-shaped cylinder. *Phys. Rev. B*, 82:125430, 2010.
[72] A. Aubry, D. Y. Lei, S. A. Maier, and J. B. Pendry. Conformal transformation applied to plasmonics beyond the quasistatic limit. *Phys. Rev. B*, 82:205109, 2010.
[73] D. Y. Lei, A. Aubry, Y. Luo, S. A. Maier, and J. B. Pendry. Plasmonic interaction between overlapping nanowires. *ACS Nano*, 5:597–607, 2011.
[74] A. Aubry, D. Y. Lei, S. A. Maier, and J. B. Pendry. Plasmonic hybridization between nanowires and a metallic surface: A transformation optics approach. *ACS Nano*, 5:3293–3308, 2011.
[75] Y. Luo, A. Aubry, and J. B. Pendry. Electromagnetic contribution to surface-enhanced raman scattering from rough metal surfaces: A transformation optics approach. *Phys. Rev. B*, 83:155422, 2011.
[76] Y. Zeng, J. Liu, and D. H. Werner. General properties of two-dimensional conformal transformations in electrostatics. *Opt. Exp.*, 19:20035–20047, 2011.
[77] R. Schinzinger and P. A. A. Laura. *Conformal Mapping: Methods and Applications*. Dover, New York, 2003.
[78] G. S. Smith and R. Barakat. Electrostatics of two conducting spheres in contact. *Appl. Sci. Res.*, 30:418–432, 1975.
[79] R. C. McPhedran and D. R. McKenzie. Electrostatic and optical resonances of arrays of cylinders. *Appl. Phys. A*, 23:223–235, 1980.
[80] R. C. McPhedran and W. T. Perrins. Electrostatic and optical resonances of cylinder pairs. *Appl. Phys. A*, 24:311–318, 1981.
[81] R. C. McPhedran and G. W. Milton. Transport properties of touching cylinder pairs and of the square array of touching cylinders. *Proc. R. Soc. A*, 411:313–326, 1987.
[82] A.V. Paley, A. V. Radchik, and G. B. Smith. Quasistatic optical response of pairs of touching spheres with arbitrary dielectric permeability. *J. Appl. Phys.*, 73:3446–3453, 1993.
[83] P. Nordlander and F. Le. Plasmonic structure and electromagnetic field enhancements in the metallic nanoparticle-film system. *Appl. Phys. B: Lasers and Optics*, 84:35–41, 2006.
[84] R. F. Oulton, V. J. Sorger, D. A. Genov, D. F. P. Pile, and X. Zhang. A hybrid plasmonic waveguide for subwavelength confinement and long-range propagation. *Nature Photon.*, 2:496–500, 2008.
[85] R. Oulton, V. J. Sorger, T. Zentgraf, R.-M. Ma, C. Gladden, L. Dai, G. Bartal, and X. Zhang. Plasmon lasers at deep subwavelength scale. *Nature*, 461:629–632, 2009.
[86] M.I. Stockman. Nanofocusing of optical energy in tapered plasmonic waveguides. *Phys. Rev. Lett.*, 93:137404, 2004.
[87] Kh.V. Nerkararyan. Superfocusing of a surface polariton in a wedge-like structure. *Phys. Lett. A*, 237:103–105, 1997.
[88] D. F. P. Pile, T. Ogawa, D. K. Gramotnev, T. Okamoto, M. Haraguchi, M. Fukui, and S. Matsuo. Theoretical and experimental investigation of strongly localized plasmons on triangular metal wedges for subwavelength waveguiding. *Appl. Phys. Lett.*, 87:061106, 2005.
[89] M. Fleischmann, P. J. Hendra, and A. J. McQuillan. Raman spectra of pyridine adsorbed at a silver electrode. *Chem. Phys. Lett.*, 26:163–166, 1974.
[90] M. G. Albrecht and J. A. Creighton. Anomalously intense Raman spectra of pyridine at a silver electrode. *J. Am. Chem. Soc*, 99:5215–5217, 1977.
[91] M. Moskovits. Surface-enhanced spectroscopy. *Rev. Mod. Phys.*, 57:783–826, 1985.
[92] P. B. Johnson and R. W. Christy. Optical constants of the noble metals. *Phys. Rev. B*, 6:4370–4379, 1972.
[93] H. Wang, D. W. Brandl, P. Nordlander, and N. J. Halas. Plasmonic nanostructures: Artificial molecules. *Acc. Chem. Res.*, 40:53–62, 2007.
[94] R. Bardhan, N. K. Grady, J. R. Cole, A. Joshi, and N. J. Halas. Fluorescence enhancement by Au nanostructures: Nanoshells and nanorods. *ACS Nano*, 3:744–752, 2009.
[95] G.W. Ford and W.H. Weber. Electromagnetic interactions of molecules with metal surfaces. *Phys. Rep.*, 113:195–287, 1984.
[96] C.H. Bohren and D.R. Huffman. *Absorption and scattering of light by small particles.* John Wiley & Sons, Inc., New York, 1983.
[97] F. Javier García de Abajo. Non local effects in the plasmons of strongly interacting nanoparticles, dimers, and waveguides. *J. Phys. Chem. C*, 112:17983–17987, 2008.
[98] J. M. McMahon, S. K. Gray, and G. C. Schatz. Optical properties of nanowire dimers with a spatially nonlocal dielectric function. *Nano Lett.*, 10:3473–3481, 2010.
[99] S. Raza, G. Toscano, A.-P. Jauho, M. Wubs, and N. A. Mortensen. Unusual resonances in nanoplasmonic structures due to nonlocal response. *Phys. Rev. B*, 84:121412, 2011.
[100] C. David and F. J. Garía de Abajo. Spatial nonlocality in the optical response of metal nanoparticles. *J. Phys. Chem. C*, 115:19470–19475, 2011.
[101] J. Zuloaga, E. Prodan, and P. Nordlander. Quantum description of the plasmon resonances of a nanoparticle dimer. *Nano Lett.*, 9:887–891, 2009.
[102] E. D. Palik. *Handbook of Optical Constants of Solids*. Academic Press, New York, 1985.
[103] J. B. Pendry. Perfect cylindrical lenses. *Opt. Exp.*, 11:755–760, 2003.
[104] B. T. Draine. The discrete-dipole approximation and its application to interstellar graphite grains. *Astrophys. J.*, 333:848–872, 1988.
[105] A. Wokaun, J. P. Gordon, and P. F. Liao. Radiation damping in surface-enhanced Raman scattering. *Phys. Rev. Lett.*, 48:957960, 1982.

[106] R. Carminati, J.-J. Greffet, C. Henkel, and J. M. Vigoureux. Radiative and non-radiative decay of a single molecule close to a metallic nanoparticle. *Opt. Commun.*, 261:368–375, 2006.
[107] F. Hao, Y. Sonnefraud, P. Van Dorpe, S. A. Maier, N. J. Halas, and P. Nordlander. Symmetry breaking in plasmonic nanocavities: Subradiant LSPR sensing and a tunable fano resonance. *Nano Lett.*, 8:3983–3988, 2008.
[108] S. Zhang, D. A. Genov, Y. Wang, M. Liu, and X. Zhang. Plasmon-induced transparency in metamaterials. *Phys. Rev. Lett.*, 101:047401, 2008.
[109] N. Verellen, Y. Sonnefraud, H. Sobhani, F. Hao, V. V. Moshchalkov, P. Van Dorpe, P. Nordlander, and S. A. Maier. Fano resonances in individual coherent plasmonic nanocavities. *Nano Lett.*, 9:1663–1667, 2009.
[110] N. Liu, L. Langguth, T. Weiss, J. Kastel, M. Fleischhauer, T. Pfau, P. Nordlander, and H. Giessen. Plasmonic analogue of electromagnetically induced transparency at the drude damping limit. *Nat. Mat.*, 8:758–762, 2009.
[111] A. Alú and N. Engheta. Cloaking a sensor. *Phys. Rev. Lett.*, 102:233901, 2009.
[112] E. Dulkeith, A. C. Morteani, T. Niedereichholz, T. A. Klar, J. Feldmann, S. A. Levi, F. C. J. M. van Veggel, D. N. Reinhoudt, M. Müller, and D. I. Gittins. Fluorescence quenching of dye molecules near gold nanoparticles: Radiative and nonradiative effects. *Phys. Rev. Lett.*, 89:203002, 2002.
[113] S. Kuhn, U. Hakanson, L. Rogobete, and V. Sandoghdar. Enhancement of single-molecule fluorescence using a gold nanoparticle. *Phys. Rev. Lett.*, 97:017402, 2006.
[114] P. Anger, P. Bharadwaj, and L. Novotny. Enhancement and quenching of single-molecule fluorescence. *Phys. Rev. Lett.*, 96:113002, 2006.
[115] V. Giannini, A. I. Fernández-Domínguez, S. C. Heck, and S. A. Maier. Plasmonic nanoantennas: Fundamentals and their use in controlling the radiative properties of nanoemitters. *Chem. Rev.*, 111:3888–3912, 2011.
[116] T. Ming, H. Chen, R. Jiang, Q. Li, and J. Wang. Plasmon-controlled fluorescence: Beyond the intensity enhancement. *J. Phys. Chem. Lett.*, 3:191–202, 2012.
[117] E. M. Purcell. Spontaneous emission probabilities at radio frequencies. *Phys. Rev.*, 69:681, 1946.
[118] V. V. Klimov and D. V. Guzatov. Strongly localized plasmon oscillations in a cluster of two metallic nanospheres and their influence on spontaneous emission of an atom. *Phys. Rev. B*, 75:024403, 2007.
[119] V. V. Klimov and D. V. Guzatov. Optical properties of an atom in the presence of a two-nanosphere cluster. *Quantum Electron.*, 37:209–230, 2007.
[120] C. Kittel. *Introduction to Solid State Physics*. Wiley, New York, 1966.
[121] A. Boardman. *Electromagnetic Surface Modes*. Wiley, New York, 1982.
[122] D. Y. Lei, A. I. Fernández-Domínguez, Y. Sonnefraud, K. Appavoo, R. F. Haglund, J. B. Pendry, and S. A. Maier. Revealing plasmonic gap modes in particle-on-film systems using dark-field spectroscopy. *ACS Nano*, doi:10.1021/nn204190e, 2012.
[123] D. R. Ward, F. Hüser, F. Pauly, J. C. Cuevas, and D. Natelson. Optical rectification and field enhancement in a plasmonic nanogap. *Nature Nanotech.*, 5:732–736, 2010.
[124] H. A. Atwater and A. Polman. Plasmonics for improved photovoltaic devices. *Nature Mater.*, 9:205–213, 2010.
[125] K. Aydin, V. E. Ferry, R. M. Briggs, and H. A. Atwater. Broadband polarization-independent resonant light absorption using ultrathin plasmonic super absorbers. *Nature Commun.*, 2:517, 2011.
[126] A. C. Atre, A. García-Etxarri, H. Alaeian, and J. A. Dionne. Toward high-efficiency solar upconversion with plasmonic nanostructures. *J. Opt.*, 14:024008, 2012.
[127] A. Campion and P. Kambhampati. Surface-enhanced Raman scattering. *Chem. Soc. Rev.*, 27:241–250, 1998.
[128] S. Nie and S.R. Emory. Probing single molecules and single nanoparticles by surface-enhanced Raman scattering. *Science*, 275:1102–1106, 1997.
[129] K. Kneipp, Y. Wang, H. Kneipp, L. T. Perelman, I. Itzkan, R. R. Dasari, and M.S. Feld. Single molecule detection using surface-enhanced Raman scattering (SERS). *Phys. Rev. Lett.*, 78:1667–1670, 1997.
[130] D. J. Bergman and M. I. Stockman. Surface plasmon amplification by stimulated emission of radiation: Quantum generation of coherent surface plasmons in nanosystems. *Phys. Rev. Lett.*, 90:027402, 2003.